Cluster Observations of Ion-Scale Magnetic Structures and their Coupling with Whistler Waves During the August 17th 2003 Substorm Event

Anna Tenerani, Olivier Le Contel, F. Califano, Patrick Robert, Dominique Fontaine, Nicole Cornilleau-Wehrlin, J.-A. Sauvaud

Cluster observations of whistler waves correlated with ion-scale magnetic structures during the 17 August 2003 substorm event

A. Tenerani,[1,2] O. Le Contel,[1] F. Califano,[3] P. Robert,[4] D. Fontaine,[4]
N. Cornilleau-Wehrlin,[4,5] and J.-A. Sauvaud[6]

Received 29 May 2013; revised 9 September 2013; accepted 10 September 2013; published 3 October 2013.

[1] We provide evidence of the simultaneous occurrence of large-amplitude, quasi-parallel whistler mode waves and ion-scale magnetic structures, which have been observed by the Cluster spacecraft in the plasma sheet at 17 Earth radii, during a substorm event. It is shown that the magnetic structures are characterized by both a magnetic field strength minimum and a density hump and that they propagate in a direction quasi-perpendicular to the average magnetic field. The observed whistler mode waves are efficiently ducted by the inhomogeneity associated with such ion-scale magnetic structures. The large amplitude of the confined whistler waves suggests that electron precipitations could be enhanced locally via strong pitch angle scattering. Furthermore, electron distribution functions indicate that a strong parallel heating of electrons occurs within these ion-scale structures. This study provides new insights on the possible multiscale coupling of plasma dynamics during the substorm expansion, on the basis of the whistler mode wave trapping by coherent ion-scale structures.

Citation: Tenerani, A., O. Le Contel, F. Califano, P. Robert, D. Fontaine, N. Cornilleau-Wehrlin, and J.-A. Sauvaud (2013), Cluster observations of whistler waves correlated with ion-scale magnetic structures during the 17 August 2003 substorm event, *J. Geophys. Res. Space Physics*, *118*, 6072–6089, doi:10.1002/jgra.50562.

1. Introduction

[2] Substorms are processes whereby energy coming from the solar wind is stored in the nightside of the magnetosphere, the magnetotail, where it is rapidly released to the plasma sheet by means of particle heating and acceleration, and, finally, partly deposited in the auroral regions via precipitating particles. This transport of energy from the Sun to the Earth's ionosphere is mediated by the coupling of the solar wind with the Earth's magnetosphere and is the outcome of several multiscale physical processes. The latter involve electric and/or magnetic field fluctuations of the magnetotail encompassing a broad range of frequencies f, i.e., $f \lesssim f_{\rm ci}$ and $f_{\rm ci} \ll f < f_{\rm ce}$ or higher, $f_{\rm ci(ce)}$ being the ion (electron) cyclotron frequency.

[3] In this paper we focus on the correlation between ion-scale magnetic structures and whistler mode waves. The former are nonlinear electromagnetic fluctuations occurring at the typical time scale $f^{-1} \approx f_{\rm ci}^{-1}$ and with typical width ℓ of the order of the ion gyroradius ρ_i and the ion inertial length d_i. The latter are electromagnetic waves which propagate in a magnetized plasma at an angle θ with respect to the mean magnetic field. They are right-handed, circularly polarized, and typically with frequency $f_{\rm ci} < f \ll f_{\rm ce}$ [*Stenzel*, 1999].

[4] Previous works have shown that, during substorms, unducted whistlers may be generated in the plasma sheet by reconnection-related processes [*Wei et al.*, 2007], as well as by electron temperature anisotropies which set in near the magnetic equator [*Le Contel et al.*, 2009] or as a consequence of betatron acceleration in flux pile-up regions [*Khotyaintsev et al.*, 2011]. Very recently, *Cao et al.* [2013] investigated the interaction between ultralow- and high-frequency waves. They identified, during a substorm event, a slow magnetosonic wave with a period of 30 s which seems to significantly influence both whistler and low hybrid wave emissions. On the other hand, space observations in the magnetosheath [*Smith and Tsurutani*, 1976; *Thorne and Tsurutani*, 1981; *Tsurutani and Smith*, 1982] and in the northern dusk magnetosphere [*Dubinin et al.*, 2007] have often reported the existence of a correlation between the occurrence of whistler waves and magnetic structures showing a magnetic field minimum. The latter have usually been interpreted as nonpropagating mirror modes.

[5] Along these lines, in the present work we selected those whistler emissions that we have observed to be ducted by propagating plasma structures during the substorm. We extend a first case study reported in *Tenerani et al.* [2012] which shows how plasma density and magnetic field inhomogeneities with $\ell \approx \rho_i, d_i$, which may be associated

[1]LPP, CNRS, Ecole Polytechnique, UPMC, St. Maur-des-Fossés, France.
[2]Jet Propulsion Laboratory, California Institute of Technology, Pasadena, California, USA.
[3]Physics Department., University of Pisa, Pisa, Italy.
[4]LPP, CNRS, Ecole Polytechnique, Palaiseau, France.
[5]LESIA, Observatoire de Paris, Meudon, France.
[6]IRAP/UPS, Toulouse, France.

Corresponding author: A. Tenerani, Jet Propulsion Laboratory, California Institute of Technology, Pasadena, CA 91125, USA. (Anna.Tenerani@jpl.nasa.gov)

2169-9380/13/10.1002/jgra.50562

to nonlinear modes, come into play as channels, or carriers, for whistlers. The aim is to give, through a detailed analysis of the most significant cases, experimental evidence of new possible mechanisms affecting both wave-particle interactions and energy balance during substorms that may efficiently be provided by ducted whistlers.

[6] In this work, we present measurements of broad band whistler emissions with amplitudes of about 0.5–0.8 nT and in the frequency range $f \approx 0.1$–$0.4 f_{ce}$. We use data sets gathered by the Cluster satellites during the 17 August 2003 substorm event. The whistler waves are observed to be trapped inside coherent structures which are embedded in a fast earthward ion flow and which exhibit magnetic field depressions and density humps. During the substorm event, the Cluster satellites are located in the magnetotail, near the magnetic equator, at a radial distance of 17 Earth radii. The intersatellite separation is about $d = 200$ km, less than the typical values of the ion gyroradius and the ion inertial length of the magnetotail, both of the order of 1000 km. In addition, the Cluster spacecraft are in high telemetry mode, allowing for waveform measurements of the magnetic and electric field fluctuations occurring at frequencies comprising between the ion cyclotron and the whistler waves ones. Thanks to the combination of high time resolution and multipoint measurements, the Cluster spacecraft data set allows for a detailed investigation of dynamical processes occurring at the electron and ion scales, as well as to inspect stationary and propagating magnetic structures at the scale of the intersatellite separation.

[7] This paper is organized as follows: in section 2 we explain the data set used; section 3 describes the global context and the main features of this substorm event; in section 4 we describe the whistler waves detected during the substorm, focusing on those which are correlated with ion-scale structures showing a magnetic field minimum and a density hump; conclusions and comments about our observations are discussed in section 5.

2. Data and Instrumentation

[8] The local magnetic field is measured by the FluxGate Magnetometer (FGM) instrument, which samples the magnetic field variations at 14.87 ms time resolution [*Balogh et al.*, 2001]. At higher frequencies, magnetic field is measured by the Spatio-Temporal Analysis of Field Fluctuations (STAFF) search coil magnetometers [*Cornilleau-Wehrlin et al.*, 2003] which measure the magnetic field fluctuations in the frequency range 0.1 Hz to 4 kHz. Onboard STAFF analyzers provide waveform data up to 225 kHz for that event (hereafter data called STAFF SC data), higher frequency data being obtained by the onboard spectrum analyzer STAFF SA. In the present study we use waveform at 2.22 ms time resolution for frequencies above 10 kHz, and FGM data for the low-frequency fluctuations and for DC magnetic field, averaging the data over the appropriate time. The waveform of the electric field is provided by the Electric Fields and Waves experiment (EFW) [*Gustafsson et al.*, 2001] at 2.22 ms resolution. Ion and electron particle data are provided by the Cluster Ion Spectrometry-Composition and Distribution Function analyzer (CIS-CODIF) [*Rème et al.*, 2001] on spacecraft 4 and the Plasma Electron And Current Experiment (PEACE) [*Johnstone et al.*, 1997] on spacecraft 2, respectively. For this event, high-energy measurements at 125 ms time resolution of electron pitch angle distribution functions, PADs for brevity, are available. In particular, the data set 3DX from the High Energy Electron Analyzer (HEEA) is used for PADs. Both ion and electron moments, such as plasma density, bulk velocity, and temperature, are available at 4 s time resolution, providing us the average plasma parameters. The spacecraft potential measured by EFW is used to display electron density fluctuations at 200 ms time resolution [*Pedersen et al.*, 2001].

[9] For the sake of clarity, the low-frequency magnetic field components from FGM will be indicated with capital letters B_x, B_y, and B_z. High-frequency magnetic field fluctuations, measured by STAFF SC, will instead be indicated with small letters b_x, b_y, and b_z. Spacecraft are represented by different colors following the usual convention: black for Cluster 1 (C1), red for Cluster 2 (C2), green for Cluster 3 (C3), and blue for Cluster 4 (C4).

[10] If not stated explicitly in the text, data are plotted in GSE coordinates. The calibrated waveform from STAFF SC shown in the following plots is high-pass filtered at 20 kHz. The displayed spectrograms are inferred from the magnetic field waveform measured by STAFF SC, high-pass filtered at 10 Hz. The time series of the spectra have been obtained from a Fourier transform of the calibrated signal carried out over sub-intervals of 14 ms time length, i.e., every 64 point measurements, which corresponds to a resolution in frequency $\Delta f = 7$ Hz. A Hanning windowing is used in the Fourier transform.

[11] As the EFW instrument measures only two components of the electric field in the spin plane, the third component E_z is calculated by assuming $\mathbf{E} \cdot \mathbf{B} = 0$, provided the magnetic field does not lie in the spin plane. The elevation angle $\theta_{elev} = \arctan(B_z/\sqrt{B_x^2 + B_y^2})$ is used as a controlling parameter for the applicability of this method. The $\mathbf{E} \cdot \mathbf{B} = 0$ approximation is rather good for those whistler mode waves which propagate in a direction very close to the background magnetic field. On the other hand, it should be kept in mind that the same approximation is likely to be less suitable for the low-frequency structures which could be responsible for the parallel electron heating as discussed later in the conclusion. The three-dimensional (3-D) EFW data provided by the CAA are obtained by following this procedure, where both EFW and FGM data in the ISR2 frame are used to perform the calculation. The limit value of the elevation angle is set at 15°, and the magnitude of the B_z component has to be larger than 2 nT. However, in order to gain more electric field data during the time intervals analyzed in this work, we have reprocessed the three-dimensional electric field using a less restrictive limit value of the elevation angle, which we set at $\theta_{elev} = 10°$. Furthermore, the calculation of the third component has been done using the magnetic field data in the GSE frame instead of the ISR2 one. As the difference between ISR2 and GSE consists only in a rotation of 2–7° degrees around the y axis, this calculation is still a good estimate of the three-dimensional electric field which has been confirmed by the comparison between our products and the CAA ones (not shown).

3. Overview of the Event

[12] On 17 August 2003 from 16:30 to 17:00 Universal Time (UT hereafter) the Cluster spacecraft, s/c hereafter,

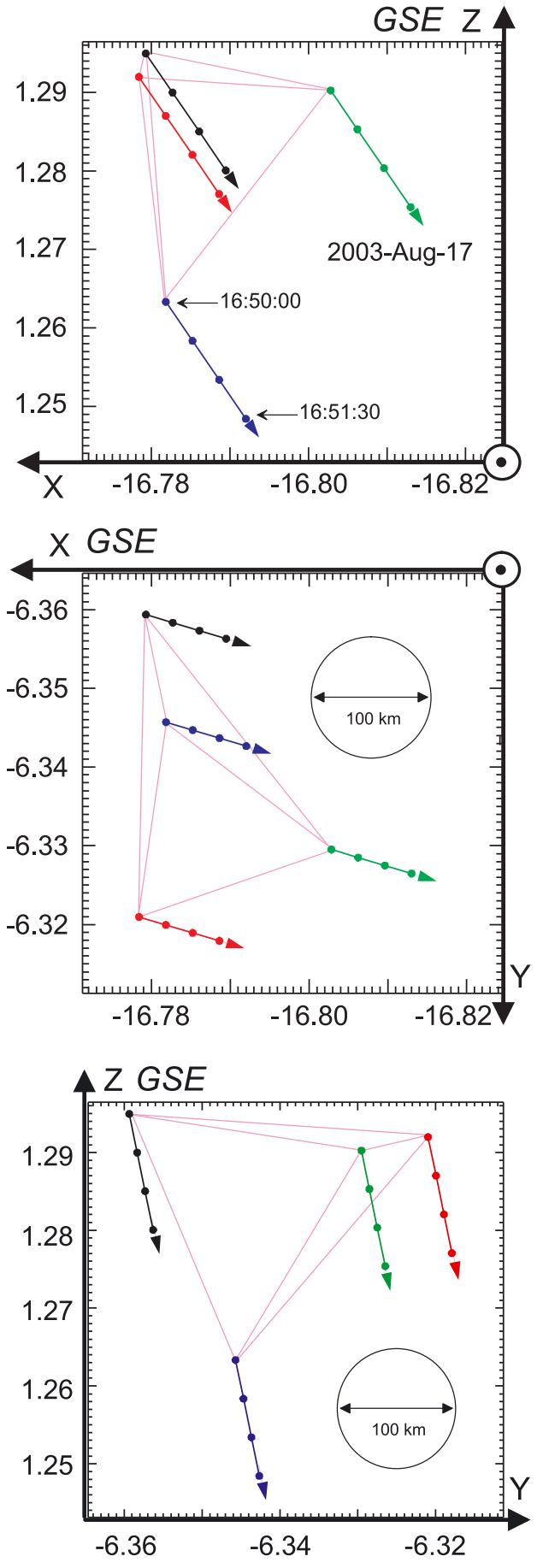

crossed the magnetotail at about 17 R_E inside the plasma sheet, near the magnetic equator, during a substorm event. Figure 1 shows the Cluster spacecraft coordinates in Earth radius units and the length scale of the tetrahedron, in GSE coordinates.

[13] The *AE* index, which is shown in Figure 2 from 15:30 to 17:30 UT, starts increasing at nearly 16:25 UT, and it reaches about 700 nT at nearly 17:00 UT, meaning that a substorm is taking place. In Figure 3 we give an overview of the event showing magnetic field and ion particle data for C4. Figure 3 (first panel) displays the three magnetic field components B_x, B_y, and B_z in black, red, and green color, respectively, measured by FGM at 4 s time resolution. Data show that the Cluster s/c cross the magnetic equator from the northern toward the southern lobe of the magnetotail at nearly 16:05 UT, as B_x changes from positive to negative values. From nearly 16:30 to 17:03 UT, during the local expansion of the substorm, Cluster detects strong magnetic field fluctuations corresponding to frequencies of the order or less than the ion cyclotron frequency (i.e., periods of oscillations from minutes up to a few seconds). In the second panel, the spectral intensity of magnetic fluctuations b_z is shown from 16:00 to 17:30 UT. A strong activity is observed starting at 16:30, seen up to 200 kHz on STAFF SC data, and up to 400 Hz by STAFF SA (not shown here). On the contrary, before 16:30 UT, in particular during the first equator crossing around 16:05 UT, the tail is quiet and no wave activity is detected. In the third panel we show the current density obtained by means of the *curlometer* technique [*Chanteur*, 1998] using FGM data from the four spacecraft: black, red, and green colors correspond to J_x, J_y, and J_z, respectively. During the first equator crossing, around 16:05 UT when the growth phase is expected to take place, the dawn-to-dusk current density J_y in the central current sheet is $J_y \approx 20\,\mathrm{nA/m^2}$. Once the substorm develops, the central plasma sheet strongly oscillates and plasma transport is greatly enhanced; see Figure 3 (last panel) where the X_{gse} component of the ion velocity $V_{i,x}$ is displayed. Ion particle data show that the ion velocity is directed tailward and earthward in the time intervals 16:33–16:52 UT and 16:55–17:03 UT, respectively, during which ions can reach speeds up to 1000 km/s. Ion fluxes are shown in the last panel.

[14] During the substorm, from 16:30 to 17:03 UT, the s/c cross the central current sheet several times. It is worth noting that the magnetic field strongly oscillates, and variations are due to both local plasma wave perturbations of the equilibrium configuration of the plasma sheet and large-scale oscillations of the tail northward and southward. We usually consider as central plasma sheet crossings those variations leading to the crossing of the magnetic equator, where $B_x = 0$. Two categories can be distinguished: (1) a quasi-neutral current sheet when $B_x = 0$, $B_y = 0$, and $B_z \neq 0$, but $B_z/B_{\mathrm{Lobe}} \ll 1$, where B_{Lobe} is the magnetic field in the lobes

Figure 1. The Cluster trajectory in GSE coordinates from 16:50:00 to 16:51:30 UT on 17 August 2003. C1, C2, C3, and C4 trajectories are plotted following the standard Cluster colors (black, red, green, and blue, respectively). Lengths are expressed in Earth radius units. The circle represents the scale length of the intersatellite separation.

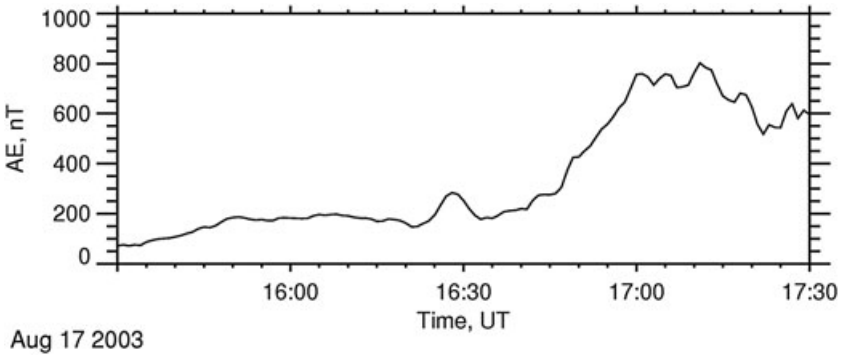

Figure 2. Auroral Electrojet index (*AE*) plotted in time interval 15:30–17:30 UT on 17 August 2003 (courtesy of Kyoto World Data Center for Geomagnetism).

and (2) a current sheet with a guide field when a large B_y component is measured at the equator.

[15] *Henderson et al.* [2006] and *Nakamura et al.* [2008] have analyzed in detail two examples of such central plasma sheet crossings during this same substorm event. Henderson et al. analyze equator crossings of the first type during the tailward ion flow. The authors associate the crossing events considered in their study to an X line traversal near

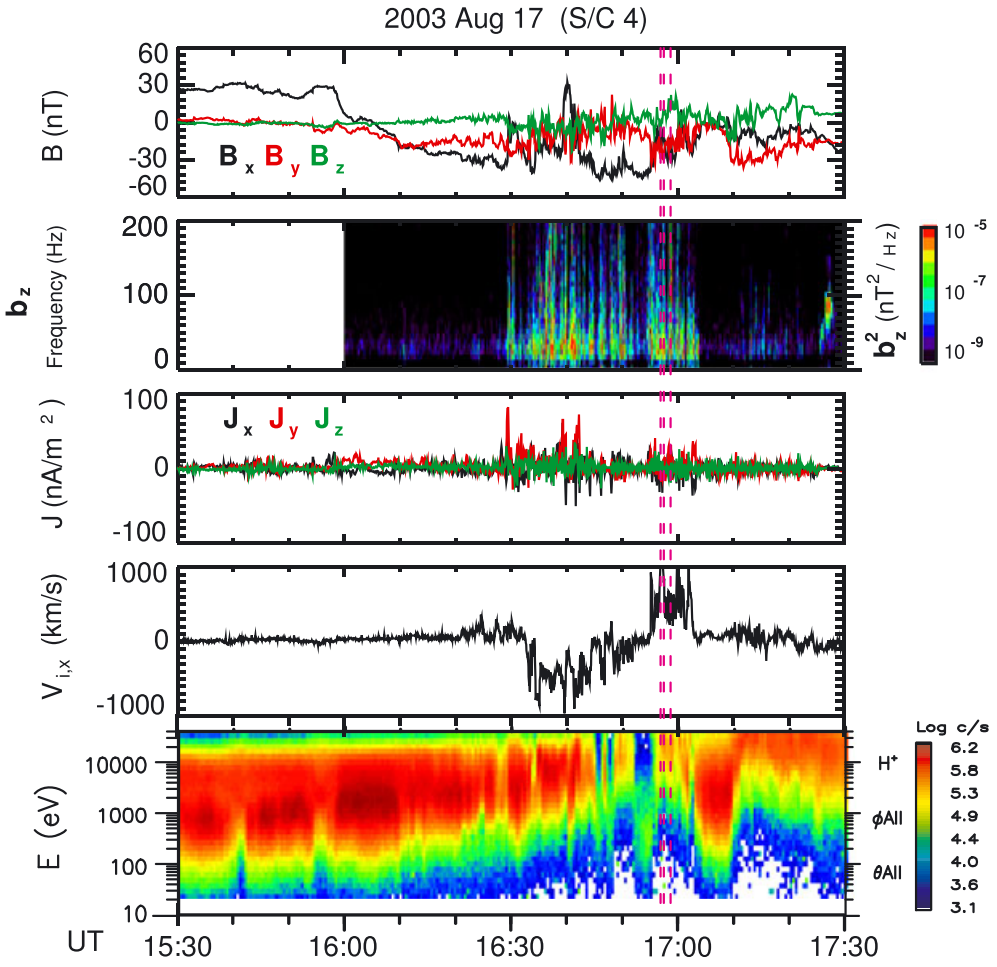

Figure 3. Magnetic field and ion particle data in GSE for C4 from 15:30 to 17:30 UT. (first panel) The three magnetic field components B_x, B_y, and B_z (FGM, 4 s time resolution); (second panel) spectral intensity of magnetic fluctuations b_z (from a Fourier transform of STAFF SC waveform from 16:00 to 17:30 UT); (third panel) current density **J** (from the *curlometer* technique); (fourth panel) X_{gse} component of the ion velocity $V_{i:x}$; (last panel) ion particle fluxes (CIS-CODIF). The red dashed lines indicate the three case studies analyzed.

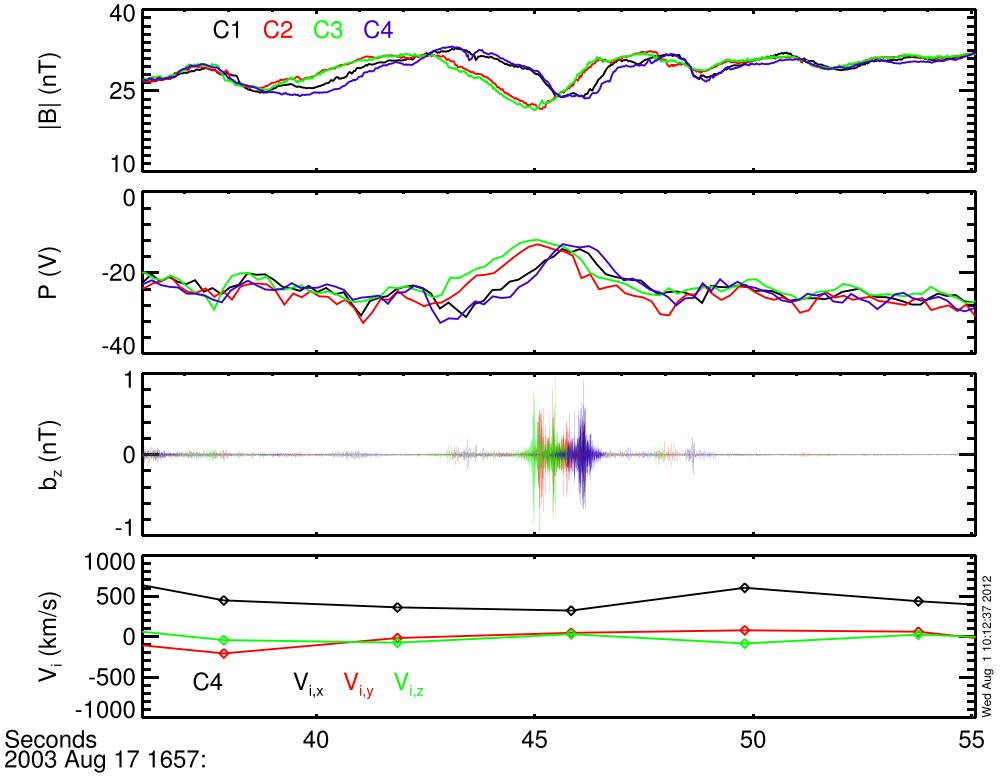

Figure 4. Case 2. (top to bottom) the magnitude of the magnetic field |**B**| (FGM); the spacecraft potential (EFW); the z component of the high-frequency magnetic field fluctuations b_z measured by each spacecraft (STAFF SC); the three components $V_{i,x}$, $V_{i,y}$, and $V_{i,z}$ of the ion velocity (black, red, and green color, respectively (CIS-CODIF)).

a reconnection site. Reconnection signatures have also been reported for this same substorm event by *Asano et al.* [2008], based on electron particle data gathered just after the flow reversal. Yet, *Nakamura et al.* [2008] analyze an equator crossing of the second type, during the earthward ion flow. This equator crossing is characterized by a strong dawn-to-dusk current J_y, $J_y \approx 100\,\mathrm{nA/m^2}$, and a strong B_y component of the tail's magnetic field. This equator crossing has not a straightforward interpretation in terms of reconnection. It is worth noting that while the latter central current sheet crossing occurs on the same time and spatial scales as our magnetic structures, no whistler waves are observed.

[16] In the following section, we will deal with large-amplitude whistler mode wave emissions and magnetic structures observed southward of the magnetic equator during the fast earthward ion flow period, by focusing on three short time intervals between 16:57 and 16:59 UT, which are represented by the vertical red dashed lines in Figure 3.

4. Whistler Wave Detection Inside Coherent Ion-Scale Structures

[17] Emissions have been selected on the basis of the following criteria: whistler waves should have large amplitudes, $|b| > 0.1$ nT; the ducting ion-scale structure must be detected by at least three spacecraft and should be detected by different spacecraft with a clear delay; we have excluded those local perturbations that may be interpreted as signatures of relative motions between the magnetotail and the s/c toward the magnetic equator. The latter correspond to those oscillations of the magnetotail leading to a decrease of the magnitude of B_x which is detected by all s/c with a specific ordering: C1, the nearest s/c to the magnetic equator, detects the smallest value of $|B_x|$; C4, the farthest s/c from the equator, detects the strongest value of $|B_x|$; and s/c in the middle, C2 and C3, detect an intermediate value. The above conditions are quite restrictive but allow for the identification of ion-scale ducting structures moving in a definite direction with respect to the Cluster s/c. Finally, the largest amplitude whistler waves have been selected because we assume that the strongest emissions are nearer to, or even in correspondence with, the source region than the weakest ones.

[18] The selected events, henceforth referred to as Case 1, Case 2, and Case 3, are detected between 16:57 and 16:59 UT, thus during the earthward ion flow. We have carried out for each case study a detailed analysis of the high-frequency wave packets, of the low-frequency perturbation and of the electron dynamics, as described below.

[19] High-frequency waves are studied by means of a polarization analysis in Fourier space by using the methods of *Means* [1972] and *Samson and Olson* [1980] in order to show that these emissions are in the whistler mode. Both spectra and polarization parameters, e.g., the propagation angle with respect to the magnetic field, are obtained from data projected in the magnetic field-aligned reference frame (MFA hereafter). By definition, the MFA reference frame is a set of orthogonal unitary vectors where the $\hat{\mathbf{z}}_{\mathrm{mfa}}$ direction

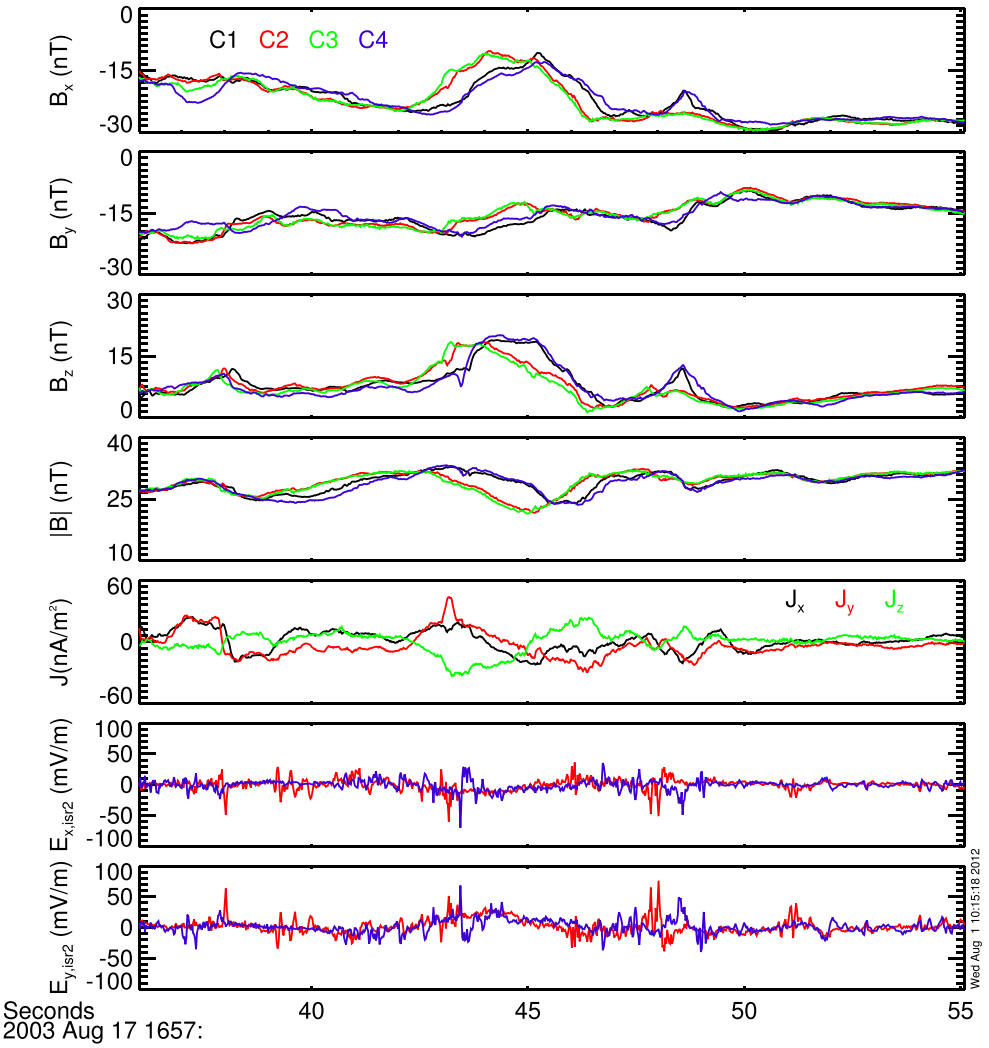

Figure 5. Case 2. (first to third panels) The three components B_x, B_y, and B_z of the magnetic field (FGM); (fourth panel) magnitude of the magnetic field $|\mathbf{B}|$ (FGM); (fifth panel) current density; (sixth and seventh panels) the two components of the electric field $E_{y,\mathrm{isr2}}$ and $E_{x,\mathrm{isr2}}$ shown in the ISR2 frame for C2 and C4, averaged over 22 ms (EFW).

is parallel to the background magnetic field while the other two directions, $\hat{\mathbf{x}}_{\mathrm{mfa}}$ and $\hat{\mathbf{y}}_{\mathrm{mfa}}$, are perpendicular. In particular, we have defined $\hat{\mathbf{x}}_{\mathrm{mfa}} = \hat{\mathbf{y}}_{\mathrm{gse}} \times \hat{\mathbf{z}}_{\mathrm{mfa}}$ and $\hat{\mathbf{y}}_{\mathrm{mfa}} = \hat{\mathbf{z}}_{\mathrm{mfa}} \times \hat{\mathbf{x}}_{\mathrm{mfa}}$. The FGM magnetic field **B**, at 14 ms time resolution, has variations on a time scale longer than the typical time scale of the whistler emissions. For this reason, the low-frequency magnetic field **B** can be considered the local background magnetic field for the purpose of defining the MFA frame for whistlers.

[20] The magnetic structures, or low-frequency perturbations, will be considered as nonlinear perturbations $\delta\mathbf{B}$ of an equilibrium magnetic field $\mathbf{B}_0$ such that $\mathbf{B} = \mathbf{B}_0 + \delta\mathbf{B}$. The average magnetic field $\mathbf{B}_0$ and the other plasma parameters, used to define the equilibrium of the low-frequency perturbations, are obtained by averaging fields over few seconds, and they will be labeled with a *zero* (e.g., B_0, J_0, and n_0). In order to carry out a comprehensive and exhaustive description of these low-frequency structures, both multispacecraft and single-spacecraft methods of data analysis have been employed. In the former case, the method of analysis of magnetic discontinuities has been used, hereafter referred to as the *timing technique*. In the latter case, the minimum variance analysis, henceforth MVA, has been employed. The timing technique assumes that a planar, or one-dimensional, structure in uniform motion crosses satellites. By using the crossing time delay of the structure between satellites and their spatial separation, the timing technique enables both the direction **n** and the speed v_0 at which the structure crosses spacecraft to be determined [*Cornilleau-Wehrlin et al.*, 2003; *Chanteur*, 1998]. With the same assumptions, the MVA allows for estimating, for a given satellite, the minimum variance direction $\hat{\mathbf{z}}_{\mathrm{mva}}$ of the magnetic field [*Sonnerup and Scheible*, 2000]. Note that, for a moving planar structure, the minimum variance direction $\hat{\mathbf{z}}_{\mathrm{mva}}$ of the magnetic field is a proxy for the normal direction **n**. As will be shown, single-spacecraft and multispacecraft methods yield, as expected, almost the same value for $\hat{\mathbf{z}}_{\mathrm{mva}}$ and **n**, respectively. For this reason, we will adopt, in the text, the same symbol **n** to indicate both the minimum variance and the normal directions. We will highlight the properties of the polarization of the

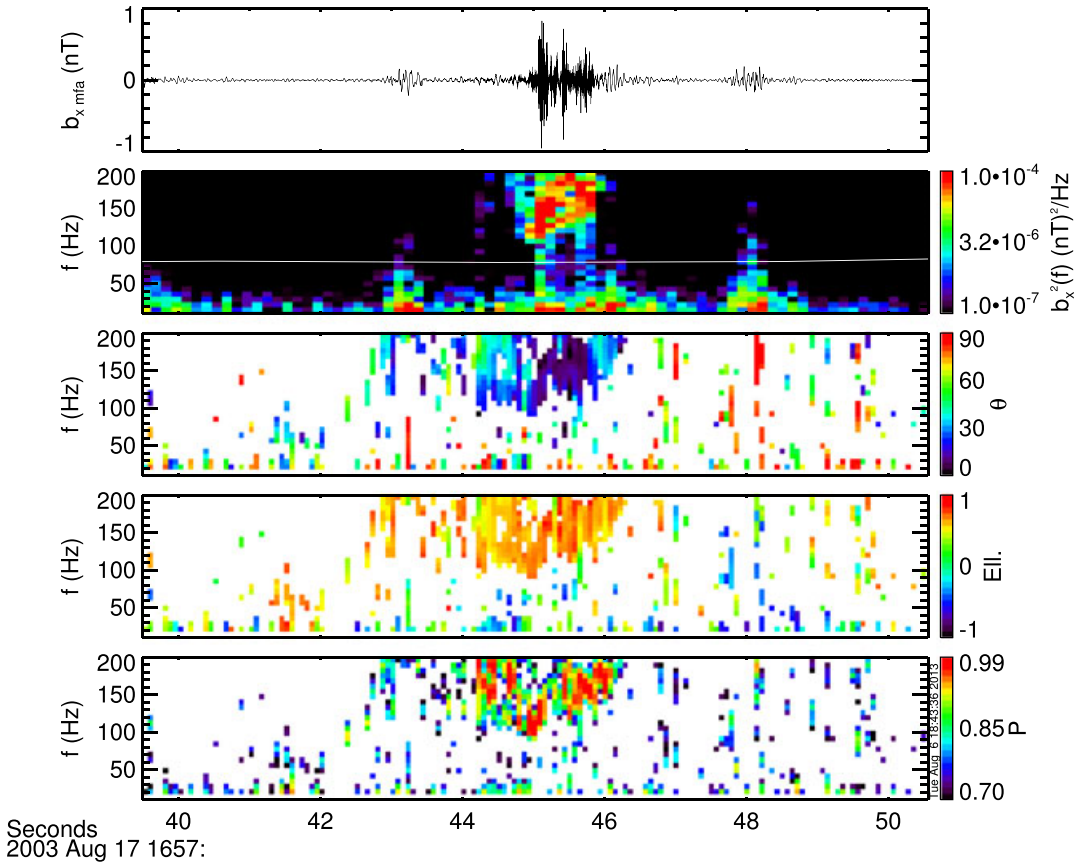

Figure 6. Case 2. Polarization analysis for C2. (top to bottom) waveform of the perpendicular component $b_{x,\mathrm{mfa}}$ of the magnetic fluctuations (STAFF SC); spectral energy density of $b_{x,\mathrm{mfa}}$, where the white line superposed corresponds to a frequency $f = 0.1 f_{ce}$; propagation angle θ; ellipticity Ell.: Ell > 0 means right-handed polarization; degree of polarization $\mathcal{P}$. In the last three panels we show polarization results corresponding to $\mathcal{P} \geq 0.7$.

structures by projecting the magnetic field $\delta\mathbf{B}$ and related fields, e.g., the current and the electric field, in both the MVA and MFA reference frames. In this case, the average magnetic field $\mathbf{B}_0$ has been used in order to define the MFA frame for the low-frequency perturbation. The magnetic field $\mathbf{B}_0$ will not be displayed for the different case studies, but it is worth mentioning that $\mathbf{B}_0$ is not constant and it is slightly inhomogeneous at the intersatellite separation length scale, as it varies slowly with time, and satellites measure different values of the average magnetic field. Thus, the structure is not strictly embedded in a homogeneous magnetic field even at the scale of the intersatellite distance.

[21] Finally, electron particle dynamics is investigated by means of pitch angle distribution functions. In particular we compared, as far as possible, the distribution functions in both the magnetic field-aligned and perpendicular directions.

[22] In subsection 4.1 we describe in detail the main case study, Case 2. Analogies and possible differences between Case 2 and the other case studies are discussed in subsection 4.2.

4.1. Main Case (Case 2)

4.1.1. Identification of the Structure

[23] Figures 4 and 5 represent data for Case 2 from 16:57:36 to 16:57:55 UT (see also *Tenerani et al.* [2012]). In Figure 4 (top to bottom), we show the magnitude of the magnetic field $|\mathbf{B}| \equiv B$, the spacecraft potential P (proportional to density fluctuations), the z component of the high-frequency magnetic field fluctuations b_z measured by each spacecraft, and the three components $V_{i,x}$, $V_{i,y}$, and $V_{i,z}$ of the ion velocity (in black, red, and green colors, respectively). The low-frequency magnetic structure is detected by the four s/c from around 16:57:42 UT to 16:57:49 UT, and it is characterized by a magnetic field depression of nearly $\delta B/B = -0.25$ (first panel) and a density increase of $\delta n/n = 0.5$ (second panel). At the minimum of the magnetic field and the maximum of the density, a large-amplitude wave packet is detected (third panel), while the ion velocity is mainly directed earthward (fifth panel). Figure 5 shows the components B_x, B_y, and B_z of the magnetic field, the magnitude B, the three components J_x, J_y, and J_z of the current density (in black, red, and green colors, respectively), and the two components of the electric field $E_{x,\mathrm{isr2}}$ and $E_{y,\mathrm{isr2}}$ in the ISR2 frame for C2 and C4. The magnetic structure, being detected with a delay by the four s/c (first four panels), is at the scale of the intersatellite separation. The current component J_z oscillates within $\pm 40\,\mathrm{nA/m^2}$, and the J_x and J_y components, after an initial increase toward positive values, show an almost symmetric profile (fifth panel) with a maximum negative value (see comments in section 4.1.3 below). Note that the two electric field components (last two panels) show bipolar signatures at the edges of the

magnetic structure which are detected with same delay, suggesting that they are associated with the propagation of the low-frequency structure itself. These secondary electromagnetic structures are at the electronic spatial scales and will not be considered in the present work.

4.1.2. Whistler Waves

[24] The spectrogram and the polarization analysis of the high-frequency wave packets are shown in Figure 6 for C2. Here we show, from top to bottom, the waveform of the perpendicular component $b_{x,\mathrm{mfa}}$ of the magnetic fluctuations, the spectral energy density of the same component (the white line superposed corresponds to one tenth of the electron cyclotron frequency which is about $f_{ce}^0 = 800$ kHz), the propagation angle θ between the wave vector and **B**, the ellipticity, and the degree of polarization $\mathcal{P}$. The ellipticity is defined as the ratio between the minor and the major axes of the ellipse transcribed by the wave components transverse to the z_{mfa} direction. A positive ellipticity indicates a right-handed polarization. The minimum value of $\mathcal{P}$ for reliable results of the polarization analysis is usually $\mathcal{P} = 0.7$, so that we show, in the last three panels, polarization results corresponding to $\mathcal{P} \geq 0.7$: as can be seen, the emission has a well-defined state of polarization with $\mathcal{P} \approx 1$ and ellipticity Ell.$\approx +1$.

[25] In summary, according to this analysis the wave packets are elliptically right-handed polarized, with frequency in the range $f = 100 - 225$ kHz, corresponding to $f = 0.1$–$0.3 f_{ce}^0$, as expected for whistler mode waves. Spectra from STAFF SA (not shown here) show that the frequency reaches nearly $f = 300$ Hz$\approx 0.4 f_{ce}^0$. The whistlers are quasi-parallel, with a propagation angle $0° < \theta < 30°$. The phase velocity of the waves v_{ph} has been estimated from the values of electric and magnetic field fluctuations perpendicular to the background magnetic field **B**, which can be obtained from waveform measurements (not shown), $v_{\mathrm{ph}} \approx e_\perp / b_\perp$ with $e_\perp \approx 5$ mV/m and $b_\perp \approx 0.5$ nT. These values yield a phase speed $v_{\mathrm{ph}} \approx 10^4$ km/s (in reasonable agreement with estimates of v_{ph} obtained from the whistler dispersion relation within the cold plasma approximation, for our frequency range).

4.1.3. Low-Frequency Structure

[26] The equilibrium quantities are obtained by averaging fields over 10 s, as the typical transit time of the structure is 5 s. The average plasma parameters are given by the magnetic field components $B_{x,0} = -25$ nT, $B_{y,0} = -15$ nT, and $B_{z,0} = 10$ nT, the magnitude of the magnetic field $B_0 = 30$ nT, the ion-scale lengths $\rho_i \approx d_i = 600$ km, the density $n_0 = 0.15\ \mathrm{cm}^{-3}$, the ion cyclotron frequency $f_{ci}^0 = 0.43$ kHz, and the ion and electron plasma beta $\beta_i = 0.67$ and $\beta_e = 0.067$, respectively (see also Table 3).

4.1.3.1. Timing Technique

[27] In order to perform the timing between s/c, we chose as a reference the time at which each s/c detected half of the minimum value of the magnitude B. The time sequence of the s/c used is 16:57:43.0.9 UT for C3, 16:57:44.1 UT for C2, 16:57:45.09 UT for C1, and 16:57:45.14 UT for C4. The crossing velocity of the structure turns out to be $v_0 = 174 \pm 16$ km/s along $\mathbf{n}_{\mathrm{gse}} = \{0.5, -0.8, -0.4\} \pm 0.1$; see also Table 1. The typical scale length of the structure ℓ can be estimated by means of the crossing velocity v_0 and the crossing time interval $\Delta T \sim 5$ s during which the perturbation is detected by each s/c. In this way we estimated $\ell \sim 900$ km, which is of the order of the ion scales ρ_i and d_i. In order to describe the low-frequency structure as purely advected by the plasma flow or as a propagating nonlinear wave, the ion velocity along the normal direction must be compared with the inferred velocity v_0. Keeping in mind the simplified model of a nonlinear wave propagating in a homogeneous plasma, the propagation velocity with respect to the plasma will be given by $V = v_0 - V_{i,n}$, where $V_{i,n}$, the ion velocity along the normal direction, must be evaluated outside the structure. Note that the magnetic field is varying over the satellite spin period, i.e., 4 s, thus particle moment calculations cannot be accurate. Furthermore, the energy of ions can exceed the maximum energy which can be detected by the ion instrument CIS-CODIF (see, for instance, the ion fluxes in Figure 3, last panel), thus leading to an underestimated ion velocity. However, we chose as a reference value for estimating the ion velocity outside the structure the last measurement point before the detection of the magnetic structure (time 16:57:38 UT), where the magnetic field is almost constant. We assume the standard value 20 km/s for the error in the ion velocity measurement and an error 0.1 for the normal direction. For this event, the estimated velocity along the normal is $V_{i,n} \approx 400 \pm 100$ km/s (see also Figure 8, fifth panel), which yields a propagation velocity $V \approx -225 \pm 116$ km/s. This result suggests that the structure is mainly propagating dawnward, in the opposite direction to the bulk flow component along the normal **n**.

4.1.3.2. Magnetic Field-Aligned Frame Analysis

[28] Figure 7 shows the normalized nonlinear perturbation $\delta\mathbf{B}/B_0$ in the MFA coordinate system, the normalized current perturbation $\delta\mathbf{J}_{\mathrm{mfa}}/J_0$ obtained from the curlometer technique, one of the two components of the raw electric field data $E_{y,\mathrm{isr2}}$ for C2 and C4 in the ISR2 frame, the inferred three-dimensional electric field $\mathbf{E}_{\mathrm{mfa}}$ for C2 and C4 (electric field data are averaged over 222 ms in order to smooth high-frequency oscillations), and the elevation angle θ_{elev} (solid lines), where we marked with a dashed line the critical value $\theta_{\mathrm{elev}} = 10°$ (see also section 2 for the definition of θ_{elev}).

[29] By inspection of plots, the perturbation $\delta\mathbf{B}$ clearly shows both a compressional component $\delta B_\parallel$ ($\delta B_{z,\mathrm{mfa}}$, Figure 7, third panel), and a strong shear component $\delta B_\perp$ ($\delta B_{y,\mathrm{mfa}}$, Figure 7, second panel). As expected from magnetic field data, the current is quasi-parallel to the magnetic field (Figure 7, fourth panel, red color), showing an almost symmetric profile. However, since the waveform in the shear component is not exactly antisymmetric in time, the $J_\parallel$ component does not show an exact symmetry with respect to the center of the structure itself. In the perpendicular directions the current is instead antisymmetric. In order to clarify the current signatures which are expected according to the observed magnetic field, in Figures 7a–7c we show empirical profiles of the magnetic field which suit to observations and the related current. For the current signature, for instance, compare the perpendicular and parallel components of **J** in Figure 7 (fourth panel), black and red colors, with Figure 7c, black and red lines, respectively. For this case study, electric field data are available over a time interval which covers more than one half of the structure. It can be clearly seen that in the perpendicular direction the same signatures as those of the magnetic field are found in the electric field $\mathbf{E}_{\mathrm{mfa}}$; see Figure 7 (sixth and seventh panels).

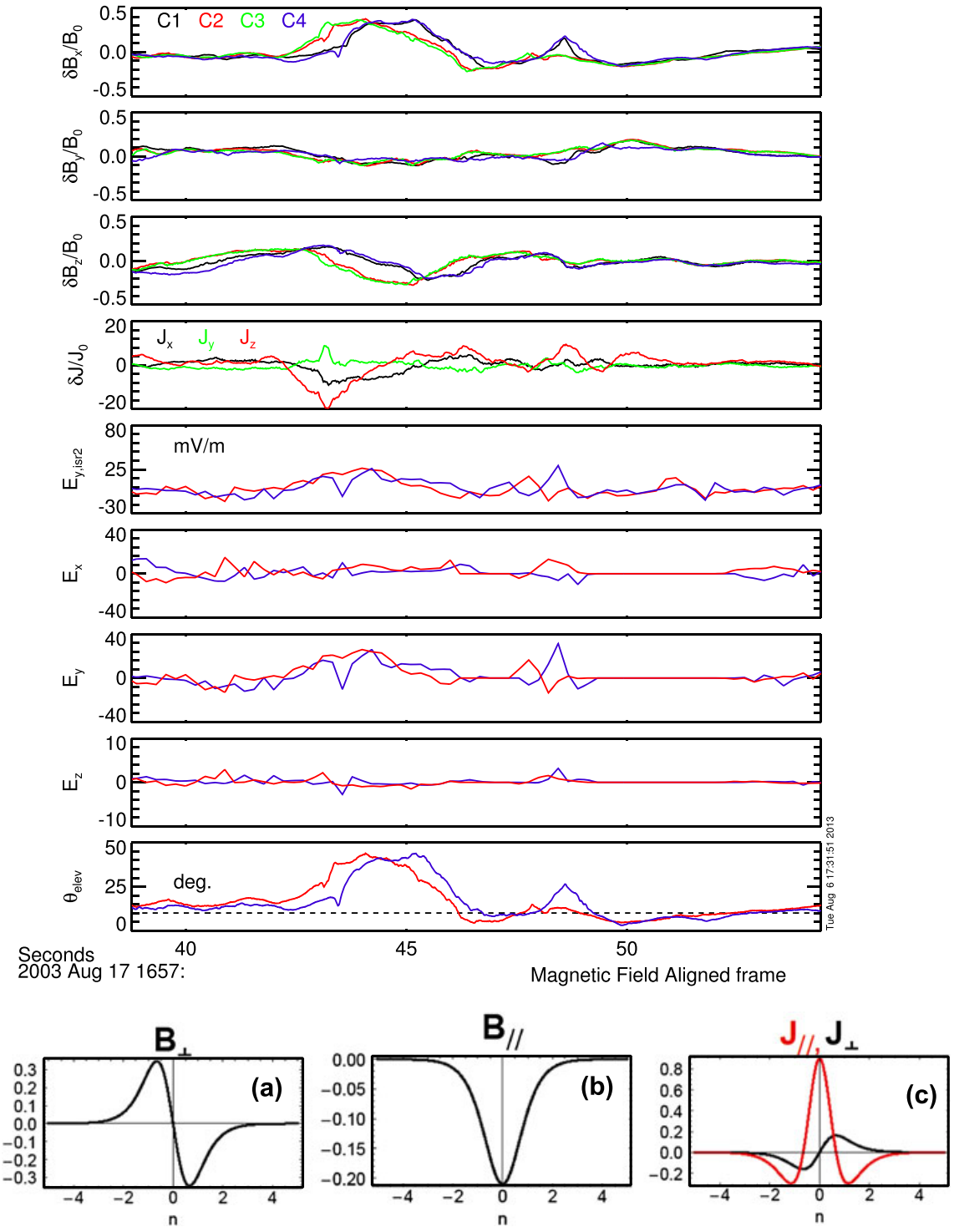

Figure 7. Case 2. Field projections in the MFA frame. (top to bottom) normalized components of the magnetic field, $\delta\mathbf{B}/B_0$ (FGM); normalized components of the current, $\delta\mathbf{J}/J_0$; raw electric field $E_{y,\mathrm{isr2}}$; components of the electric field **E** (EFW, averaged over 222 ms); elevation angle θ_{elev}, solid lines, and the critical value $\theta_{\mathrm{elev}} = 10°$, dashed line. (a–c) An empirical magnetic field waveform in the parallel and perpendicular directions and the related current profile.

4.1.3.3. Minimum Variance Analysis

[30] The MVA has been applied to $\delta\mathbf{B}/B_0$ in the time intervals 16:57:43–16:57:48.5 UT for C1 and C4, and 16:57:42–16:57:47.6 UT for C2 and C3. We determined the minimum variance direction, n_x, n_y, and n_z being its GSE components. The same MVA for both $\delta\mathbf{B}/B_0$ and the total magnetic field **B**, not shown here, lead to similar results. As a consequence, even if the background is not homogeneous, the structure turns out to be well defined and isolated from the background itself. In Table 1 the values of n_x, n_y, and n_z are listed

Table 1. Results of the MVA and Timing Technique Analysis for Each s/c[a]

	s/c	n_x	n_y	n_z	λ_{max}	λ_{int}	λ_{min}
Case 1	C1	0.357	–0.257	0.898	0.038	0.020	0.003
	C2	0.336	–0.305	0.890	0.035	0.018	0.003
	C3	0.204	–0.296	0.908	0.043	0.016	0.003
	Timing N/A						
Case 2	C1	0.489	–0.775	–0.411	0.05	0.008	3×10^{-4}
	C2	0.373	–0.864	–0.339	0.06	0.008	6×10^{-4}
	C3	0.385	–0.873	–0.300	0.06	0.008	5×10^{-4}
	C4	0.475	–0.849	–0.231	0.047	0.01	4×10^{-4}
	Timing	0.5 ± 0.1	-0.8 ± 0.1	-0.4 ± 0.1			
Case 3	C1	0.234	–0.741	–0.629	0.072	0.052	0.018
	C2	0.305	–0.562	–0.769	0.082	0.076	0.0194
	C3	0.249	–0.589	–0.768	0.077	0.062	0.0194
	C4	0.275	–0.837	–0.473	0.066	0.042	0.0163
	Timing	0.3 ± 0.2	-0.7 ± 0.1	-0.6 ± 0.1			

[a]The components of the normal in GSE coordinates, the maximum, intermediate, and minimum variances λ_{max}, λ_{int}, and λ_{min}, respectively, are listed.

for each s/c. The maximum, intermediate, and minimum variance values, λ_{max}, λ_{int}, and λ_{min}, respectively, are also listed. The MVA results are consistent with an almost 1-D structure, since the maximum, intermediate, and minimum variances satisfy $\lambda_{max}/\lambda_{int} \gtrsim 2$ and $\lambda_{int}/\lambda_{min} \gg 1$. The inferred normal is quasi-perpendicular, at an angle $\Theta \approx 80°$ with respect to the average magnetic field $\mathbf{B}_0$. A comparison between the normal inferred from both the timing technique and the MVA shows that these two methods are in good agreement, yielding, for this case, a normal directed mainly along the Y_{gse} direction.

[31] Figure 8 shows fields projected in the MVA frame relative to C4. From top to bottom we plot the normalized maximum, intermediate, and minimum variance components of the magnetic perturbation $\delta\mathbf{B}_{mva}/B_0$ (δB_{max}, δB_{int}, and δB_{min}, respectively), the normalized current perturbation $\delta\mathbf{J}_{mva}/J_0$ (black, red, and green colors correspond to the current in the maximum, intermediate, and minimum variance directions, respectively), the $\mathbf{E} \times \mathbf{B}$ drift along the normal for C2 and C4, averaged at 4 s (solid lines), and the ion velocity $V_{i,n}$ (dot-dashed line); the electric field, and the elevation angle for C2 and C4 in the last panel. In this time interval we are near the threshold condition for the three-dimensional calculation of the electric field (see the elevation angle), so that the averaged $\mathbf{E} \times \mathbf{B}$ drift does not match the absolute values of the ion velocity, as expected for low-frequency dynamics. Nevertheless, their trend is in reasonable agreement. As for the MFA frame, we show here one perpendicular component of the raw data, $E_{y,\,isr2}$, and the three electric field components along the maximum, intermediate, and minimum variance directions (electric field data are averaged over 222 ms). In this case, the electric field along the normal direction shows a clear anticorrelation with δB_{max}, as expected for highly oblique waves. In agreement with the MFA analysis, it is possible to clearly identify a shear antisymmetric component of the magnetic field perturbation given by δB_{max} and a compressive, symmetric component represented by δB_{int}. The current signature as well has an antisymmetric profile in the maximum variance direction (black color) and an almost symmetric profile in the intermediate variance direction (red color). With regard to this, compare with the empirical waveform of the magnetic field and the correspondent current profile shown in Figures 8a–8c.

[32] According to the present analysis, to a good approximation we can consider the low-frequency perturbation a 1-D structure, propagating in a direction quasi-perpendicular to the average magnetic field $\mathbf{B}_0$. The perturbation has a typical length scale of the order of the ion scales, and it has both a compressive and a shear component propagating at a speed much less than the whistler phase speed, in the $(X, Y)_{gse}$ plane. In this way, the slowly propagating low-frequency perturbation is seen as an almost static inhomogeneity by whistlers, which in turn can be efficiently ducted.

4.1.4. Particles

[33] Figure 9 represents the time evolution of the electron PADs. In particular, we show the PADs in the directions perpendicular and aligned to the magnetic field, provided data along these two directions are available simultaneously. Note that at this time resolution the spacecraft do not complete one spin so that only partial information about the electron distribution function can be extrapolated. Nevertheless, as the magnetic field changes significantly over few seconds, snapshots of the electron PADs provide important information about their time evolution when crossing the magnetic structure.

[34] Figure 9 (first and second panels) represents the magnetic field data: the first panel shows the magnitude B of the magnetic field, and the second panel the b_z component of the whistler waves detected by C2. Each symbol superposed to B corresponds to a specific type of electron PAD, and it is represented as many times as each kind of PAD has been observed. In Figures 9a–9h, the most representative PAD samples for each type are displayed, in chronological order. The latter are shown before, during, and after the magnetic structure has passed past the s/c. Since the magnetic field is almost constant outside the structure, in this way it is possible to identify the typical PADs of the background equilibrium and how they change inside the structure.

[35] The first remarkable feature is that electrons are highly energetic, with energies exceeding 10 keV, and PADs can be classified as flat-top distributions inside the structure. These types of distributions are characterized by a plateau

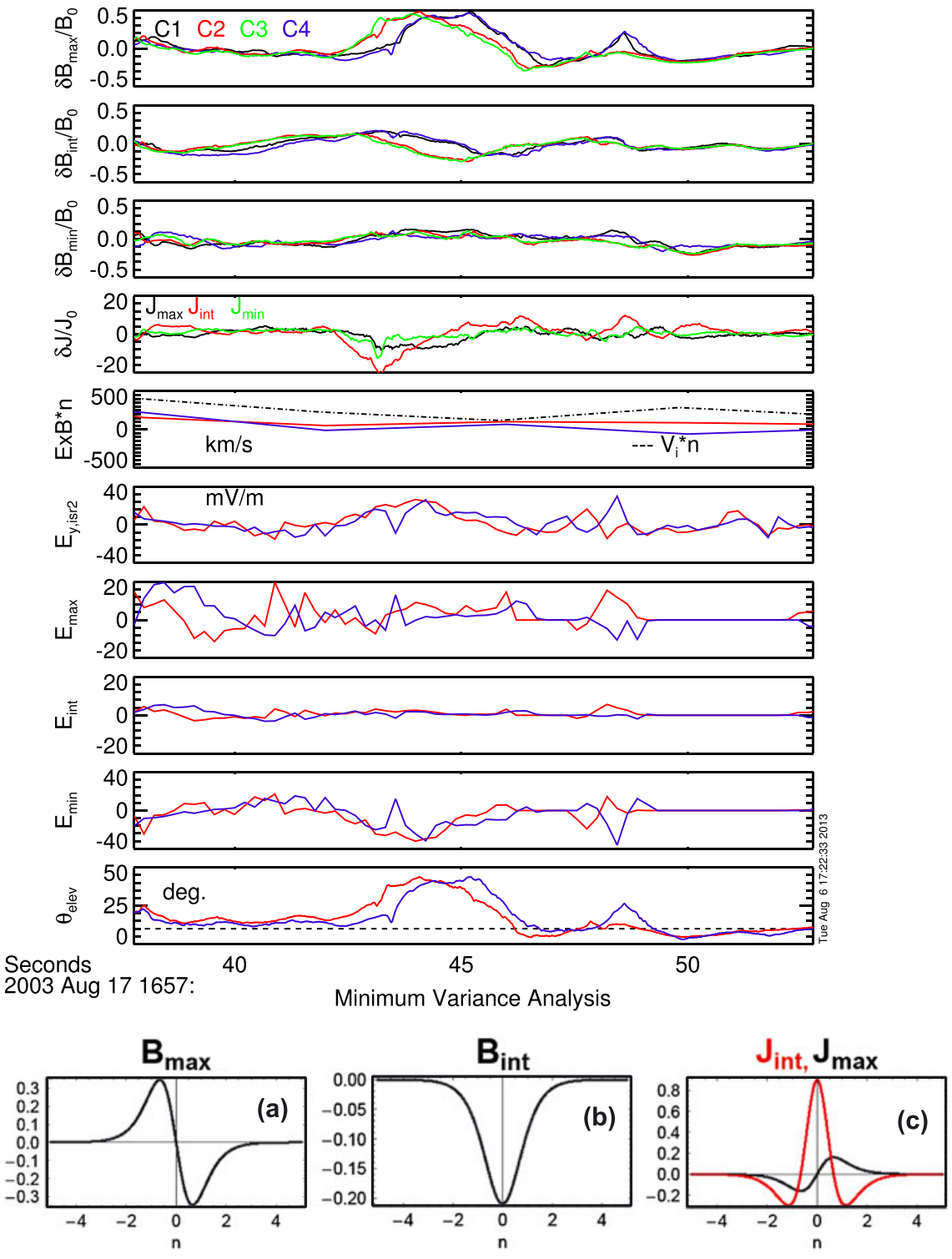

Figure 8. Case 2. Field projections in the MVA frame relative to C4. (top to bottom) Components of $\delta\mathbf{B}_{\mathrm{mva}}/B_0$ (FGM); current perturbation $\delta\mathbf{J}/J_0$; ion velocity $V_{i,n}$ (CIS-CODIF), dotted line, and the $\mathbf{E}\times\mathbf{B}$ drift along the normal averaged at 4 s (EFW and FGM); raw electric field $E_{y,\mathrm{isr2}}$; 3-D inferred electric field $\mathbf{E}$ (EFW, averaged over 222 ms); elevation angle. (a–c) Analogous to Figures 7a–7c.

of the phase space density at high energies (typically in the energy range E = 1–5 keV) which steeply decreases at the so-called shoulder energy. Flat tops are usually interpreted as a signature of the ion diffusion region which forms at a reconnection site [*Shinohara et al.*, 1998; *Nagai et al.*, 1998, 2001; *Asano et al.*, 2008], since they are often detected during ion fast flows ($V_{i,x}$ > 300–400 km/s), and possibly they exhibit signatures which are consistent with the Hall current [*Nagai et al.*, 2001]. However, the generation mechanism of such distributions and how they

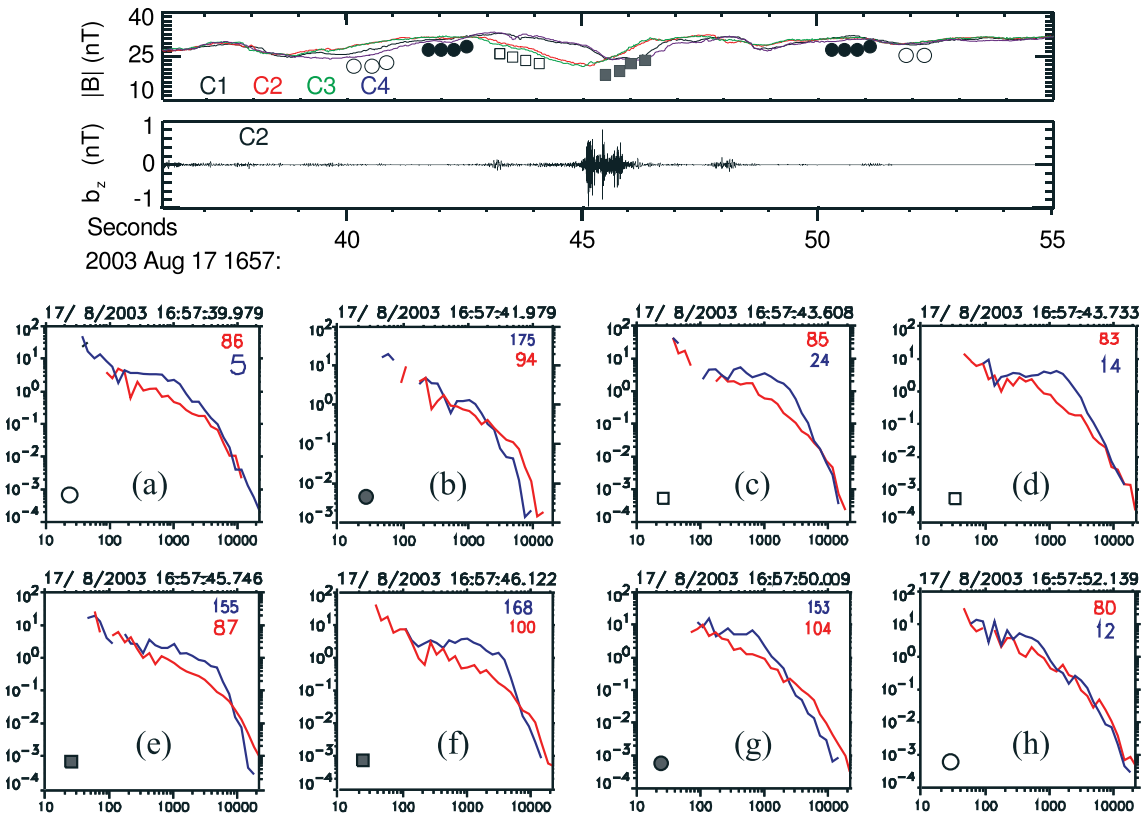

Figure 9. Case 2. Magnetic field and electron pitch angle distributions. (first panel) Magnitude |**B**| of the magnetic field (FGM); (second panel) b_z component of the high-frequency fluctuations (STAFF SC). (a–h) Selected snapshots of the electron distribution function for C2 (PEACE-HEEA 3DX data set). The number density f(km^6/s^3) is plotted versus the energy E (eV) in the magnetic field-aligned and perpendicular directions. For each snapshot, the numbers at the top right corner correspond to two selected values of the pitch angle.

are related to magnetic reconnection is still an open issue [*Asano et al.*, 2008]. *Asano et al.* [2008] carried out a statistical study of flat-top distribution functions and, as already mentioned, report flat-top distributions also during this substorm event, just after the ion flow reversal at nearly 16:55:15 UT, 2 min before the detection of our magnetic structure.

[36] Here PADs have been classified into four types: no flat top in the parallel and perpendicular directions and a not significant $T_{\perp,e} > T_{\|,e}$ anisotropy, empty circle; no flat top in the antiparallel and perpendicular directions and an anisotropy $T_{\perp,e} > T_{\|,e}$, solid circle; flat top in the parallel direction and a not significant $T_{\perp,e} > T_{\|,e}$ anisotropy, empty rectangle; flat top in the antiparallel direction and a $T_{\perp,e} > T_{\|,e}$ anisotropy, solid rectangle.

[37] Outside the structure PADs are not of the flat-top type. In addition, PADs show more particles in the parallel direction, thus equatorward, than in the antiparallel one at energies $E > 3$ keV. This can be seen by comparing the number density of PADs in the field-aligned directions outside the structure. In particular, compare samples shown in Figures 9a and 9b, observed before the crossing of the structure, and samples shown in Figures 9g and 9h, which are observed after the crossing of the magnetic structure. Inside the structure, flat-top distributions in the field-aligned direction are observed at energies $0.2 \lesssim E \lesssim 4$ keV. In addition, a $T_{\perp,e} > T_{\|,e}$ anisotropy is strongly marked in the antiparallel/perpendicular directions. This anisotropy yields a higher number of particles in the perpendicular direction than in the antiparallel one at energies $E > 10$ keV, which correlates well with the whistler emission (Figures 9f and 9e, solid rectangles). On the contrary, in the parallel/perpendicular directions it is not always clear (Figures 9c and 9d, empty rectangles).

[38] The correlation of the strong PAD anisotropy $T_\perp/T_\|$ with the low-frequency structure is consistent with the detection of large-amplitude whistler waves. In the simple case of a bi-Maxwellian distribution, a configuration with an electron temperature anisotropy $T_{\perp,e} > T_{\|,e}$ may be unstable for resonant interaction with perturbations in the whistler mode, the so-called *whistler anisotropy instability* [*Gary and Madland*, 1985]. The energy of low-frequency electrons which resonate with whistler waves can be written as [*Kennel and Petschek*, 1966]

$$E_R = E_m \frac{\omega_{ce}}{\omega}\left(1 - \frac{\omega}{\omega_{ce}}\right)^3, \qquad (1)$$

where $E_m = B^2/2\mu_0 n$ is the magnetic energy per particle. For given density $n = 0.15$ cm^{-3}, magnetic field magnitude $B = 30$ nT and frequencies 0.1–$0.4 f_{ce}^0$, equation (1) roughly yields $E_R = 81$–110 keV, in agreement with the observed

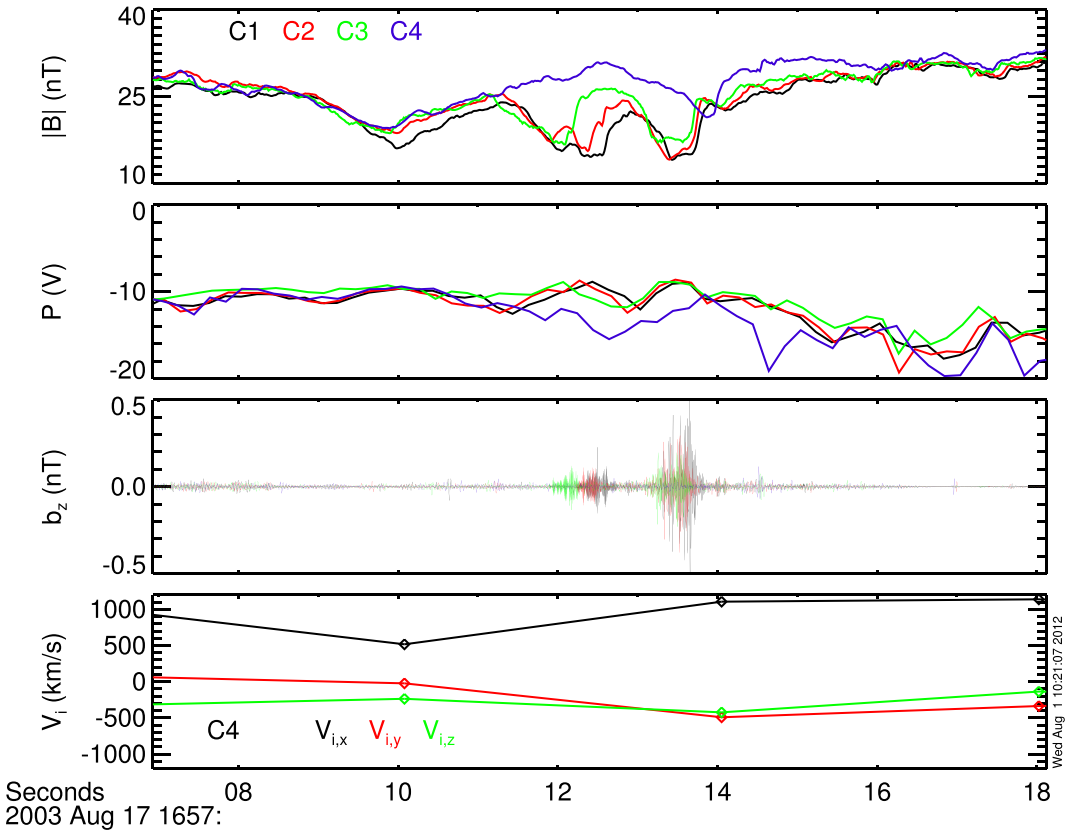

Figure 10. Case 1. Same format as Figure 4.

energy range where more particles in the perpendicular direction are observed. Note that this is an excess estimate of the resonant energy since in magnetic troughs and density humps E_R is lower. In this way more particles can resonate and enhance the growth of whistlers [*Thorne and Tsurutani*, 1981; *Li et al.*, 2011a; *Li et al.*, 2011b]. In addition, *inside* the magnetic structure the plasma beta is higher with respect to the background. It has been shown that the threshold for the onset of the whistler anisotropy instability decreases with increasing electron plasma beta [*Gary and Wang*, 1996]. This fact and the effective decrease of E_R may explain the generation of whistlers inside the structure, while outside they are not observed even in presence of a temperature anisotropy.

[39] To summarize the salient features, the PADs outside the structure do not show flat-top distributions. Flat tops, found in the field-aligned direction, correlate well with the magnetic structure. In addition, a $T_{\perp,e} > T_{\parallel,e}$ anisotropy is found within the structure yielding more particles in the perpendicular direction than in the field-aligned one at energies $E > 10$ keV, which is of the order of the electron resonant energy and may provide the free energy for the growth of the observed whistlers. The growth of whistler waves inside the magnetic structure may therefore be due to the contribution of two effects: the electron anisotropy and the simultaneous increase of the plasma beta.

4.2. Other Examples

[40] In Figures 10–11, with the same format as Figure 4, we show the other two case studies, namely, Case 1 (at time interval 16:57:07–16:57:18 UT) and Case 3 (at time interval 16:58:39–16:58:55 UT). Again, in these case studies the whistler waves are very well correlated with the magnetic field depression and the density increase, which is at the scale of the intersatellite separation. The main results of the analysis previously described for Case 2 still hold for both Case 1 and Case 3. In Table 1 we list the results obtained from both the MVA and timing technique for the three case studies. In Tables 2, 3, and 4 we summarize the results of the whistler polarization analysis, the average plasma parameters, and the parameters which characterize the low-frequency structures, respectively. Even if the three events are closely similar, some comments are worthwhile. A first difference concerns Case 1, where the timing technique could not be employed since only three s/c detect the magnetic structure. In this case we roughly estimated the propagation speed with respect to the s/c by evaluating $\Delta r_{1,3}/\Delta T_{1,3}$, where $\Delta r_{1,3} \approx 130$ km is the separation between C1 and C3 along the normal direction averaged over the three s/c, and $\Delta T_{1,3} \approx 0.5$ s the time delay between C1 and C3 in the detection of the first magnetic field minimum. In this way, the inferred crossing speed is $v_0 \approx 260$ km/s along the normal, which is oriented in the sense C3 $\rightarrow$ C1 of propagation, mainly along the Z_{gse} direction. Projection of the ion velocity along the averaged normal yields a value $V_{i,n}$ smaller than the error $V_{i,n} = 20 \pm 40$ km/s. Nevertheless, we used this value to roughly estimate the propagation velocity in the plasma rest frame; see results in Table 1. Another difference concerns Case 3. While in Case 1 and Case 2 the minimum variance was at least an order of magnitude smaller than the intermediate one, in Case 3 λ_{min} is only smaller than λ_{int} by about a factor 2

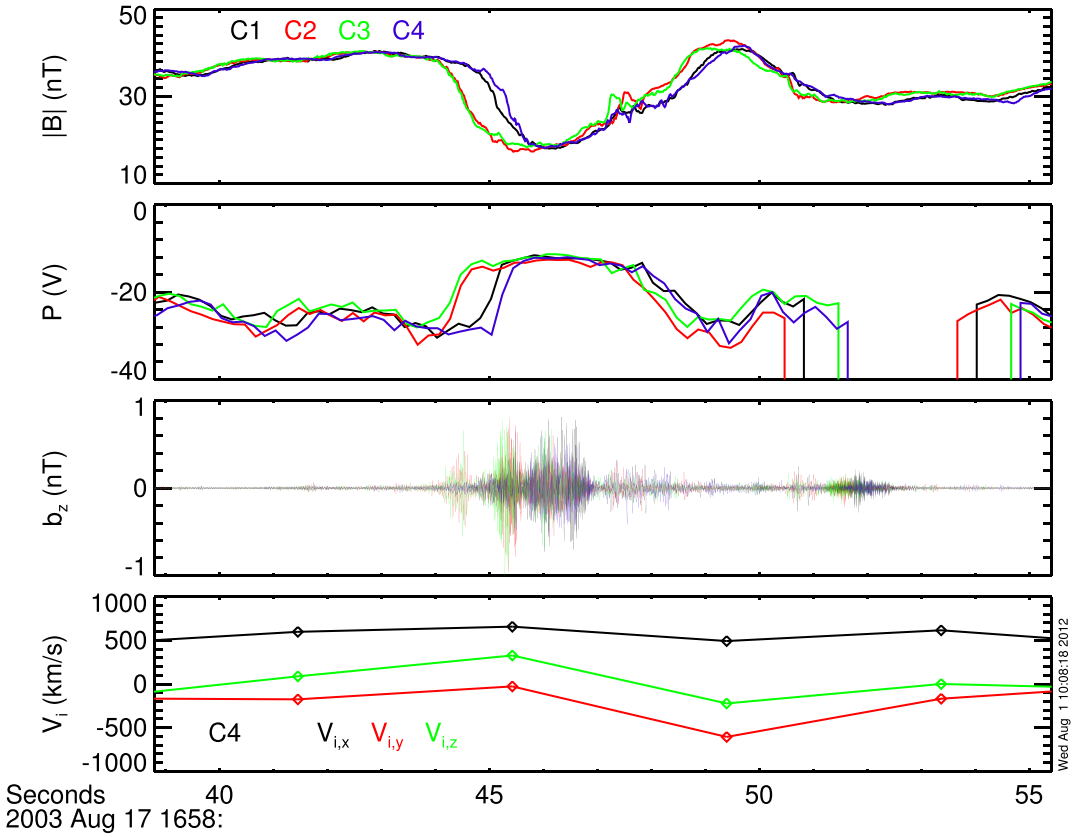

Figure 11. Case 3. Same format as Figure 4.

or 3. This suggests that the structure is more likely at least 2-D at the scale of the spacecraft separation. Nevertheless, a somewhat preferred direction of the gradient has been inferred to be quasi-perpendicular to the average magnetic field, lying in the $(Z, Y)_{gse}$ plane. Also, because of the large experimental error, the propagation velocity with respect to the bulk flow could not be determined for Case 3. The latter case study provides us a typical example of departure from the idealized case of a 1-D structure embedded in a homogeneous background. Even if the MVA does not change if we include the average magnetic field $\mathbf{B}_0$, it is reasonable that both background inhomogeneity, although weaker than the inhomogeneity of the low-frequency structure, and magnetic field line curvature play a role in shaping the magnetic structures at scales larger than the intersatellite distance. Information about the large-scale magnetic field configuration of the plasma sheet are not available from these measurements, so that we can only speculate about the possible connection of our structures to the global magnetic environment. The fact that the structures could be converging along the field line direction, like in a bottle-like configuration, is suggested by Case 3, where at the end of the structure a magnetic compression is detected. This signature would be detected if the s/c crossed the structure obliquely, thus explaining both the larger spatial scale detected (the s/c stay longer in the central part of the structure) and the less marked minimum variance.

[41] In Figures 12 and 13 we show electron PADs for Case 1 and Case 3, respectively, in the same format as Figure 9. As in the previous PADs analysis, we show samples for each specific distribution function and how they map into the magnetic field signatures. Again, in these case studies PADs are found to be anisotropic during the whistler

Table 2. Whistler Wave Parameters for the Three Case Studies[a]

	Case 1	Case 2	Case 3
$\lvert b\rvert$ (nT)	0.5	0.8	0.8
v_{ph} (km/s)	(no **E** data)	10^4	$(1-2)\times 10^4$
f/f^0_{ce}	0.1–0.3	0.1–0.4	0.1–0.4
θ	0°–30°	0°–30°	0°–40°
E_R (keV)	75–10	110–8	110–8
$E_{T_{\perp,e}>T_{\parallel,e}}$ (keV)	> 8	> 10	> 8

[a]In the last row we list the observed threshold energy corresponding to a $T_\perp/T_\parallel$ anisotropy in the electron distribution functions.

Table 3. Average Plasma Parameters for the Three Case Studies[a]

	Case 1	Case 2	Case 3
$B_{0,x}$ (nT)	–15	–25	–20
$B_{0,y}$ (nT)	–25	–15	–15
$B_{0,z}$ (nT)	5	10	15
$\lvert\mathbf{B}_0\rvert$ (nT)	25	30	34
β_i, β_e	0.67, 0.067	0.67, 0.067	0.67, 0.067
f^0_{ce} (Hz)	700	800	950
$V_{i,x}$ (km/s)	1000	500–600	500–600
c_s (km/s)	1000	1000	1000
v_a (km/s)	1600	1600	1600
n_0 (cm^{-3})	0.15	0.15	0.15
ρ_i (km)	600	600	600

[a]Coordinates are in GSE. c_s is the sound speed and v_a the Alfvén speed.

Table 4. Parameters of the Low-Frequency Structures for the Three Case Studies[a]

	Case 1	Case 2	Case 3
n (GSE)	(0.33, –0.29, 0.899)	(0.5, –0.75, –0.4)	(0.34, –0.7, –0.6)
Θ	80°	80°	100°
v_0 (km/s)	260	174	274
$V_{i,n}$ (km/s)	20 ± 40	400 ± 100	380 ± 180
$\|V\|$ (km/s)	240	225	not determined
ℓ (km)	520–780	900	1000
$\delta B/B$	–0.4	–0.25	–0.5
$\delta n/n$	0.3	0.5	0.56

[a] v_0, $V_{i,n}$, and $|V|$ are the crossing speed of the structure, the ion bulk velocity along the normal, and the propagation speed of the structure in the plasma rest frame, respectively.

emissions, with more particles in the perpendicular direction than in the field-aligned one at high energies, namely, for energies $E > 8$ keV, which is still of the same order of the resonant energies for electrons E_R at threshold. This can be seen for instance in Figures 12d and 13f–13h for Cases 1 and 3, respectively. A remarkable difference between Case 1 and Cases 2 and 3, instead, is given by PADs outside the low-frequency perturbations. In Case 1 electrons are much more highly energetic than in the other two events, with energies $E \gg 10$ keV, and they show marked isotropic flat tops in the energy range $0.5 < E < 8$ keV, both inside and outside the structure. On the contrary, for Case 3, as well as for Case 2, flat tops in the field-aligned direction are clearly correlated with the magnetic structure. This can be seen, for instance, in the sudden change of the parallel PAD when entering the structure, by comparing Figure 13b with Figure 13c. As a consequence, in Cases 2 and 3 the heating in the parallel and antiparallel directions of the magnetic field seems to be related to the ion-scale structures. On the other hand, the fact that the ion flow is faster in Case 1 could suggest that in the latter the structure is detected closer to a larger scale ion acceleration region.

5. Conclusions

[42] The case studies we have analyzed in this work occur in almost the same conditions. Typical quantities, which describe the background environment where the structures are observed, are the ion and electron plasma beta $\beta_i = 0.67$ and $\beta_e = 0.067$, the particle density $n_0 = 0.15\,\mathrm{cm}^{-3}$, and the magnetic field magnitude $|\mathbf{B}_0| = 30$ nT. Magnetic field and particle measurements show that the magnetic structures are observed when the Cluster s/c are located southward of the magnetic equator during a fast earthward ion flow ($V_{i,x} > 300$ km/s) and in regions with closed magnetic field lines. The latter property is suggested by the fact that $B_{x,0} \approx -25$ nT and $B_{z,0} \approx 10$ nT, respectively, and that

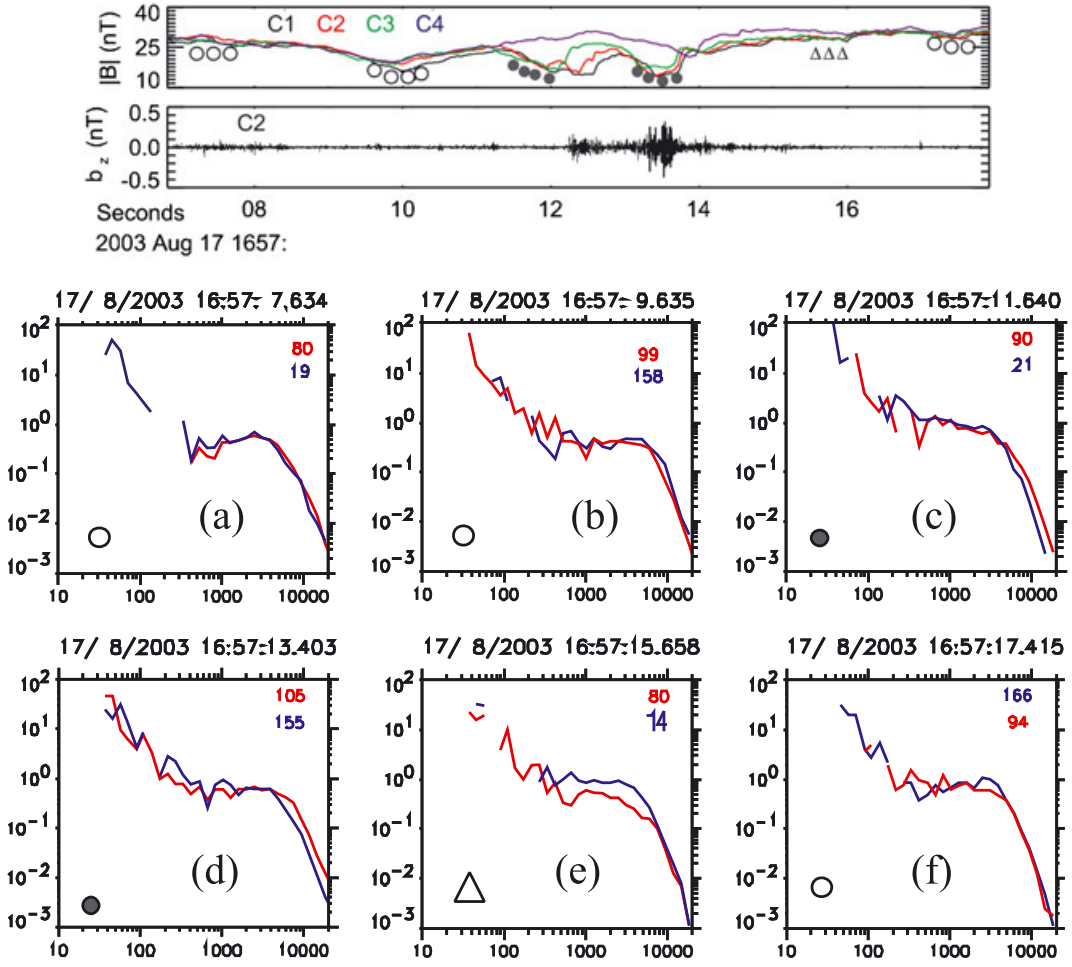

Figure 12. Case 1. Same format as Figure 9.

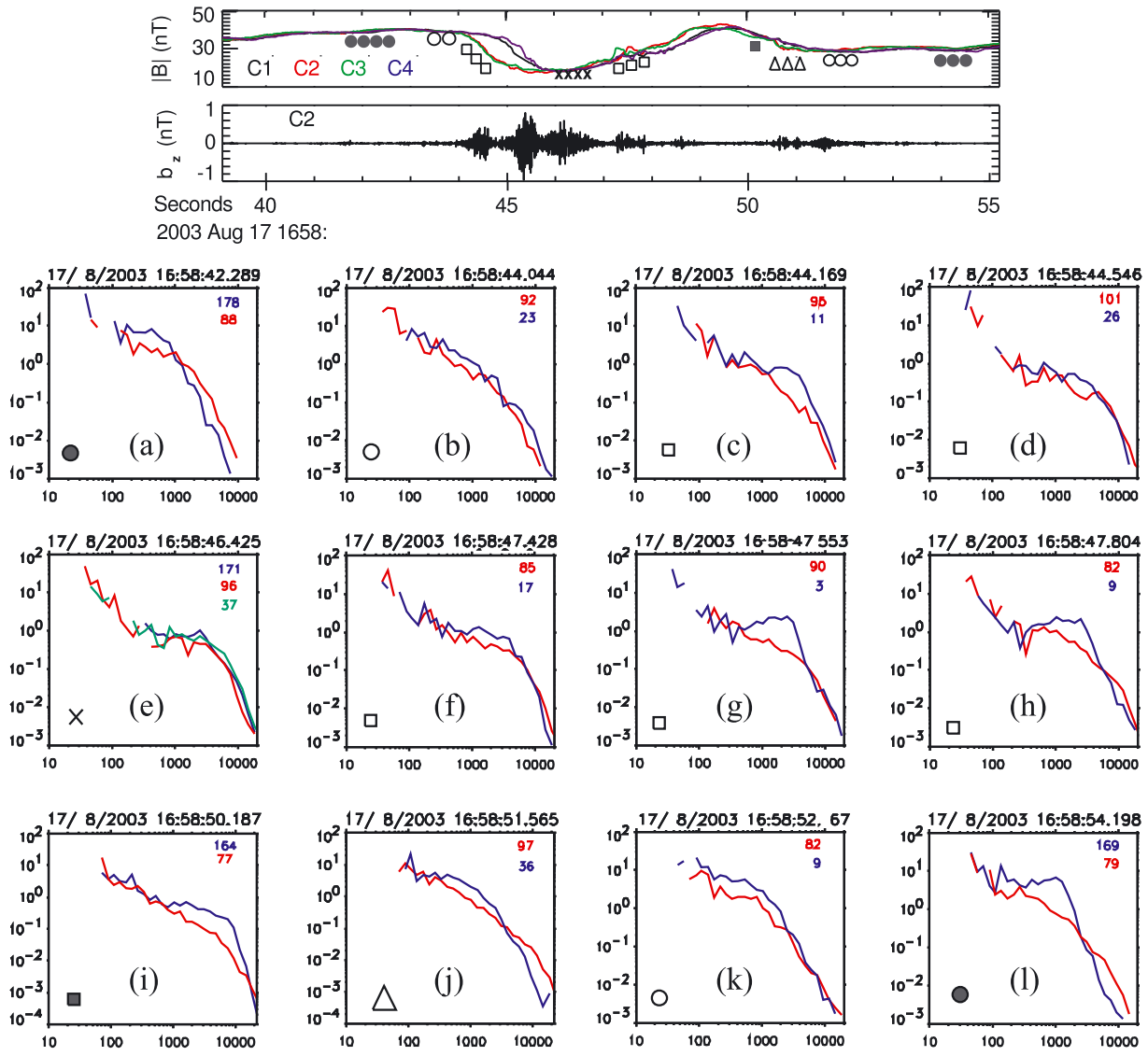

Figure 13. Case 3. Same format as Figure 9.

high-energy electrons reaching energies $E > 1$ keV are detected. The observed whistlers have amplitude of about $b = 0.5$–0.8 nT, and they propagate in a direction quasi-parallel to the background magnetic field **B**, at angles $0° < \theta \lesssim 30°$. Frequencies are in the range $0.1 < f/f_{ce}^0 \lesssim 0.4$.

[43] The correlation between the whistler wave emissions and the magnetic structures shows the main features which denote whistler ducted propagation. The magnetic structures are indeed characterized by both a density hump and a magnetic field minimum, and they are, to a good approximation, one-dimensional structures with the gradient *quasi*-perpendicular to the average magnetic field ($\Theta \approx 80°$–$100°$). The frequency of the whistlers detected inside these structures is mainly lower than one half the average electron cyclotron frequency, $f/f_{ce}^0 < 1/2$, and it is known that at these frequencies whistler waves can be trapped by stationary density humps [*Smith et al.*, 1960; *Karpman and Kaufman*, 1981; *Streltsov et al.*, 2006]. On the other hand, the observed structures are clearly not *purely* perpendicular to the average magnetic field but rather show a far richer pattern. This is characterized by a nonvanishing parallel current and by a shear component in addition to the compressive one, and, in addition, these structures propagate at a finite speed in the plasma rest frame, which has been estimated to be of the order of $|V| \approx 100$–200 km/s. Nevertheless, it has been shown that nonlinear perturbations of the slow type in a high beta plasma, and propagating slowly with respect to the whistler waves, are able to trap and advect the whistler themselves thanks to their compressive component [*Tenerani et al.*, 2012]. We thus model the magnetic structures as nonlinear, low-frequency perturbations of the slow type (i.e., with magnetic field magnitude in opposition of phase with the density perturbation), propagating quasi-perpendicular to the average magnetic field, at the ion spatial scales $\ell \sim k_\perp^{-1} \sim \rho_i, d_i$. In the framework of this interpretation, the low-frequency perturbations can be classified as nonlinear kinetic Alfvén waves, because of the length scales at play, $\ell \sim \rho_i, d_i$, and because of the type of polarization, $\delta B_\perp \gtrsim \delta B_\parallel$. It is known indeed that, at least during the linear regime, the shear kinetic Alfvén wave couples with

the slow mode if the plasma beta is of the order unity, so that a compressive component arises [*Hollweg*, 1999]. The low-frequency structures we have considered could be interpreted, within the context of the strongly inhomogeneous magnetotail, as the nonlinear development of current sheet eigenmodes [*Zelenyi et al.*, 2009].

[44] All satellites detect the trapped whistlers while the confining structure propagates. This suggests that the source is either correlated with the structure itself or at least is active for a long time with respect to the structure transit time. With regard to this, electron pitch angle distribution functions show the proper conditions for the onset of the whistler anisotropy instability to occur inside the structures. Indeed, at energies $E \gtrsim 10$ keV, which are of the order of the electron resonant energy for the whistler frequency range considered, Cluster records an enhancement of particles in the perpendicular direction with respect to the field-aligned direction. In addition, since the plasma beta increases inside the structures, the generation of whistlers by a local electron temperature anisotropy $T_{\perp,e} > T_{\parallel,e}$ is favored. Moreover, a couple of recent papers [*Li et al.*, 2011a; *Li et al.*, 2011b] on whistler chorus emissions based on observations from the THEMIS mission showed that density humps increase the fraction of resonant electrons by reducing the value of the resonant energy (see equation (1)). In the present observations, following the same rationale, both density humps and magnetic field troughs concur to decrease the value of the resonant energy and therefore to increase the linear growth rate of the whistler anisotropy instability. This fact was also emphasized in the context of whistler wave emissions in the northern dusk magnetosphere [*Dubinin et al.*, 2007] and in the magnetosheath [*Thorne and Tsurutani*, 1981].

[45] In summary, the slow-type ion-scale coherent structures increase the whistler instability linear growth rate leading to trapped large-amplitude waves. In addition, the formation of flat-top electron PADs in the field-aligned direction correlates well with the detection of the structures, at least for Cases 2 and 3. Further investigation should be carried out in order to study possible kinetic effects and wave-particle interaction between alfvénic-type perturbations and electrons leading to electron parallel heating.

[46] Trapping and transport of whistlers may play a crucial role in regulating the electron precipitations in the ionosphere. Indeed, the ion-scale structures prevent whistler energy to spread by spatially confining waves. In this way, strong pitch angle scattering of the electrons is favored, as the diffusion coefficient in phase space scales with the whistler energy amplitude. As a consequence, if whistler waves scatter particles efficiently into the loss cone, they enhance electron precipitations in the ionosphere, where electron energy is dissipated through collisions with the neutral atoms. The diffusion coefficient D resulting from wave-particle scattering can be estimated by following the theory developed by *Kennel and Petschek* [1966],

$$D = (e^2/m_e^2)\frac{\omega/\omega_{ce}}{1+2\omega/\omega_{ce}} b_\omega^2, \qquad (2)$$

where b_ω is the spectral energy density. As explained in *Kennel and Petschek* [1966], the diffusion strength in the loss cone is parametrized by $z_0^2 = \alpha_0^2/(DT_E)$, where $\alpha_0 \approx 1°$ is the halfwidth of the loss cone calculated at the equator and $T_E \approx 2.4$ s is approximately one quarter of the electron bounce period between the two hemispheres, which we estimated at a distance of nearly 17 R_E from the Earth ($T_E \approx 1/4 \times 17\, R_E$ km/10^7 km s^{-1}, where 10^7 km s^{-1} is the estimated parallel velocity of the resonant electrons). The diffusion is strong or weak for small or large values of z_0, respectively. With typical values $\omega/\omega_{ce}=0.1$ and $b_\omega^2 = 10^{-4}$ nT^2/Hz, the diffusion coefficient and the parameter z_0 turn out to be $D \approx 0.25$ Rad^2/Hz and $z_0 \approx 5 \times 10^{-4} \ll 1$, respectively. The estimated values correspond to the regime of strong diffusion into the loss cone. As demonstrated recently by *Nishimura et al.* [2010] for chorus emissions in the near-Earth region, these intense whistler mode emissions may be related to small-scale auroral structures. Although in the present observations the mapping between the farther magnetotail and the auroral region is more difficult due to the stretching of the magnetic field lines and the highly nonstationary regime, these large-amplitude ducted whistler mode waves could be the source of moving auroral patches (in azimuth along Y_{gse} or in latitude along Z_{gse}).

[47] However, the importance of such multiscale structures for the substorm physics depends on their statistical weight. Unfortunately, in the context of the Cluster mission, a statistical study is strongly limited by the following main constraints: (i) the intersatellite distance in the magnetotail was equal to 200 km only in 2003, (ii) the STAFF SC waveform is not always sampled in high burst mode, and (iii) few substorms were detected when both (i) and (ii) conditions were fulfilled. We note that, conversely, the four spacecraft of the Magnetospheric Multiscale (MMS) mission [*Burch and Drake*, 2009] in an equatorial orbit, which will be launched in 2014, will be separated by 10 to 100 km, will gather electromagnetic waveforms up to 500 Hz through the magnetotail including the parallel electric field, and will measure electron and ion distribution functions with 30 ms and 150 ms time resolution, respectively. It is therefore expected that the characterization of the multiscale structures we have studied in this article will be hopefully corroborated and completed, together with a study about their statistical importance, with the data collected by the future MMS mission.

[48] **Acknowledgments.** We are pleased to acknowledge the Cluster Active Archive and PIs for providing the experimental data. This work was done prior to A. Tenerani's employment at the Jet Propulsion Laboratory, California Institute of Technology.

[49] Masaki Fujimoto thanks Andris Vaivads and an anonymous reviewer for their assistance in evaluating this paper.

References

Asano, Y., et al. (2008), Electron flat-top distributions around the magnetic reconnection region, *J. Geophys. Res.*, *113*, A01207, doi:10.1029/2007JA012461.

Balogh, A., et al. (2001), The cluster magnetic field investigation: Overview of in-flight performance and initial results, *Ann. Geophys.*, *19*, 1207–1217.

Burch, J. L., and J. F. Drake (2009), Reconnecting magnetic fields, *Am. Sci.*, *97*(5), 392, doi:10.1511/2009.80.392.

Cao, J. B., X. H. Wei, A. Y. Duan, H. S. Fu, T. L. Zhang, H. Rème, and I. Dandouras (2013), Slow magnetosonic waves detected in reconnection diffusion region in the Earth's magnetotail, *J. Geophys. Res. Space Physics*, *118*, 1659–1666, doi:10.1002/jgra.50246.

Chanteur, G. (1998), Spatial interpolation for four spacecraft: Theory, in *Analysis Methods for Multi-Spacecraft Data,* vol. ISSI Scientific Report SR-001, edited by G. Paschmann and P. W. Daly, 349–369, International Space Science Institute, Bern, Switzerland.

Cornilleau-Wehrlin, N., et al. (2003), First results obtained by the Cluster STAFF experiment, *Ann. Geophys.*, *21*, 437–456.

Dubinin, E. M., et al. (2007), Coherent whistler emissions in the magnetosphere—Cluster observations, *Ann. Geophys.*, *25*, 303–315.

Gary, S. P., and C. D. Madland (1985), Electromagnetic electron temperature anisotropy instabilities, *J. Geophys. Res.*, *90*(A8), 7607–7610, doi:10.1029/JA090iA08p07607.

Gary, S. P., and J. W. Wang (1996), Whistler instability: Electron anisotropy upper bound, *J. Geophys. Res.*, *101*(A5), 10,749–10,754, doi:10.1029/96JA00323.

Gustafsson, G., et al. (2001), First results of electric field and density observations by Cluster EFW based on initial months of operation, *Ann. Geophys.*, *19*, 1219–1240, doi:10.5194/angeo-19-1219-2001.

Rème, H., et al. (2001), First multispacecraft ion measurements in and near the Earth's magnetosphere with the identical Cluster ion spectrometer (CIS) experiment, *Ann. Geophys.*, *19*, 1303–1354, doi:10.5194/angeo-19-1303-2001.

Henderson, P. D., et al. (2006), Cluster PEACE observations of electron pressure tensor divergence in the magnetotail, *Geophys. Res. Lett.*, *33*, L22106, doi:10.1029/2006GL027868.

Hollweg, J. V. (1999), Kinetic Alfvén wave revisited, *J. Geophys. Res.*, *104*(A7), 14,811–14,819, doi:10.1029/1998JA900132.

Johnstone, A. D., et al. (1997), PEACE: A plasma electron and current experiment, *Space Sci. Rev.*, *79*, 351–398.

Karpman, V. I., and R. N. Kaufman (1981), Tunneling transformation of whistler waves in an inhomogeneous plasma, *Sov. Phys. JETP*, *80*, 1845–1858.

Kennel, C. F., and H. E. Petschek (1966), Limit on stably trapped particles, *J. Geophys. Res.*, *71*(1), 1–28, doi:10.1029/JZ071i001p00001.

Khotyaintsev, Y., C. M. Cully, A. Vaivads, M. André, and C. J. Owen (2011), Plasma jet braking: Energy dissipation and nonadiabatic electrons, *Phys. Rev. Lett.*, *106*, 165,001, doi:10.1103/PhysRevLett.106.165001.

Le Contel, O., et al. (2009), Quasi-parallel whistler mode waves observed by THEMIS during near-Earth dipolarizations, *Ann. Geophys.*, *27*, 2259–2275.

Li, W., R. M. Thorne, J. Bortnik, Y. Nishimura, and V. Angelopoulos (2011a), Modulation of whistler mode chorus waves: 1. Role of compressional Pc4-5 pulsations, *J. Geophys. Res.*, *116*, A06205, doi:10.1029/2010JA016312.

Li, W., J. Bortnik, R. M. Thorne, Y. Nishimura, V. Angelopoulos, and L. Chen (2011b), Modulation of whistler mode chorus waves: 2. Role of density variations, *J. Geophys. Res.*, *116*, A06206, doi:10.1029/2010JA016313.

Means, J. D. (1972), Use of three-dimensional covariance matrix in analyzing the polarization properties of plane waves, *J. Geophys. Res.*, *77*(28), 5551–5559, doi:10.1029/JA077i028p05551.

Nagai, T., et al. (1998), Structure and dynamics of magnetic reconnection for substorm onsets with Geotail observations, *J. Geophys. Res.*, *103*(A3), 4419–4440, doi:10.1029/97JA021900.

Nagai, T., et al. (2001), Geotail observations of the Hall current system: Evidence of magnetic reconnection in the magnetotail, *J. Geophys. Res.*, *106*(A11), 25,929–25,949, doi:10.1029/2001JA900038.

Nakamura, R., et al. (2008), Cluster observations of an ion-scale current sheet in the magnetotail under the presence of a guide field, *J. Geophys. Res.*, *113*, A07S16, doi:10.1029/2007JA012760.

Nishimura, Y., et al. (2010), Identifying the driver of pulsating aurora, *Science*, *330*, 81–84, doi:10.1126/science.1193186.

Pedersen, A., et al. (2001), Four-point high time resolution information on electron densities by the electric field experiments (EFW) on Cluster, *Ann. Geophys.*, *19*, 1483–1489, doi:10.5194/angeo-19-1483-2001.

Samson, J. C., and J. V. Olson (1980), Some comments on the descriptions of the polarization states of waves, *Geophys. J. R. Astron. Soc.*, *61*, 115–129, doi:10.1111/j.1365-246X.1980.tb04308.x.

Shinohara, I., et al. (1998), Low-frequency electromagnetic turbulence observed near the substorm onset site, *J. Geophys. Res.*, *103*(A9), 20,365–20,388, doi:10.1029/98JA01104.

Smith, R. L., R. A. Helliwell, and I. W. Yabroff (1960), A theory of trapping of whistlers in field-aligned columns of enhanced ionization, *J. Geophys. Res.*, *65*(3), 815–823, doi:10.1029/JZ065i003p00815.

Smith, E. J., and B. T. Tsurutani (1976), Magnetosheath lion roars, *J. Geophys. Res.*, *81*(13), 2261–2266, doi:10.1029/JA081i013p02261.

Sonnerup, B., and M. Scheible (2000), *Analysis Methods for Multi-Spacecraft Data,* Chapter 8, edited by G. Paschmann and P. W. Daly, ESA Publications Division Keplerlaan, 1, 2200 AG Noordwijk, The Netherlands. 1.1 electronic ed.

Stenzel, R. L. (1999), Whistler waves in space and laboratory plasmas, *J. Geophys. Res.*, *104*(A7), 14,379–14,395, doi:10.1029/1998JA900120.

Streltsov, A. V., M. Lampe, W. Manheimer, G. Ganguli, and G. Joyce (2006), Whistler propagation in inhomogeneous plasma, *J. Geophys. Res.*, *111*, A03216, doi:10.1029/2005JA011357.

Tenerani, A., F. Califano, F. Pegoraro, and O. Le Contel (2012), Coupling between whistler waves and slow-mode solitary waves, *Phys. Plasmas*, *19*, 052103, doi:10.1063/1.4717764.

Tenerani, A., et al. (2012), Coupling between whistler waves and ion-scale solitary waves: Cluster measurements in the magnetotail during a substorm, *Phys. Rev. Lett.*, *109*, 155,005.

Thorne, R. M., and B. T. Tsurutani (1981), The generation mechanisms for magnetosheath lion roars, *Nature*, *293*, 384–386, doi:10.1038/293384a0.

Tsurutani, B. T., and E. J. Smith (1982), Lion roars and nonoscillatory drift mirror waves in the magnetosheath, *J. Geophys. Res.*, *87*(A8), 6060–6072, doi:10.1029/JA087iA08p06060.

Wei, X. H., et al. (2007), Cluster observations of waves in the whistler frequency range associated with magnetic reconnection in the Earth's magnetotail, *J. Geophys. Res.*, *112*, A10225, doi:10.1029/2006JA011771.

Zelenyi, L. M., et al. (2009), Low frequency eigenmodes of thin anisotropic current sheets and Cluster observations, *Ann. Geophys.*, *27*, 861–868.